MASTER THESIS

David Vokrouhlický

Structure and evolution of stars deformed by a nearby companion

Institute of Theoretical Physics

Prague 2023

I declare that I carried out this master thesis independently, and only with the cited sources, literature and other professional sources. It has not been used to obtain another or the same degree.

I understand that my work relates to the rights and obligations under the Act No. 121/2000 Sb., the Copyright Act, as amended, in particular the fact that the Charles University has the right to conclude a license agreement on the use of this work as a school work pursuant to Section 60 subsection 1 of the Copyright Act.

In . . . . date . . . .
                                                        Author's signature

Title: Structure and evolution of stars deformed by a nearby companion

Author: David Vokrouhlický

Institute: Institute of Theoretical Physics

Supervisor: doc. Mgr. Ondřej Pejcha, Ph.D., Institute of Theoretical Physics

Abstract: Tidal field from a nearby binary companion affects the structure and evolution of stars. We successfully applied the Kippenhahn averaging formalism to the Roche potential and used the method to formulate approximate models of tidally deformed primaries in close binary systems. We considered both the detached and the contact configurations and neglected chemical composition evolution. These tidally deformed models are thermally stable. We explored the parametric dependence of the results on three quantities: mass ratio q in the binary, surface equipotential C of the primary or the fill-out factor $F(C)$, and mass M_1 of the primary.

We found that the depth of the surface convective layer of low mass primaries increased due to tidal deformation. All models decreased their effective temperature when compared to their spherical counterparts. Our results also predict a positive correlation between the effective temperature and the fill-out factor for contact systems. Furthermore, the temperature negatively correlates with the mass ratio of the deformed system. Finally, when isolating the tidal deformation effects, a jump in temperatures was found around $1.2\,M_\odot$ for most fill-out factors. These findings could help to explain the observationally reported dichotomy of contact binary systems at the temperature approximately corresponding to the Kraft break known from isolated star population.

Keywords: contact binary stars, tidal deformation, stellar structure

Contents

Introduction

Pairs of stars that appear close together in the sky have been known since Ptolemy 2000 years ago. However, the question of why this happens, whether these stars interact, remained unexplained until the beginning of the 19$^{\text{th}}$ century. Still, in 1767, the English philosopher John Michell employed statistical methods to the by-then substantial number of double stars known and wrote: "We may from hence, therefore with the highest probability conclude... that the stars are really collected together in clusters in some places, where they form a kind of systems, whilst in others, there are either few or none of them, to whatever cause this may be owing, whether to their mutual gravitation, or to some other law or appointment of the Creator" (see Tenn [2013]).

It was William Herschel, a well-established musician (primarily during the days), and most acknowledged astronomer (primarily during the nights) who, in 1803, discovered that the Castor system (α Gemini) consists of two stars moving round each other due to their mutual gravitational interaction. Herschel observed other similar systems and concluded that all of them were stars orbiting around each other—the binary stars, as he was the first to call them in this way. After Herschel a number of other leading scientists like F. Bessel, G. Struve, O. Struve, H. Russell, and H. Shapley contributed much to the present understanding of classical binaries.

It is outside the scope of this thesis to follow rich aspects of formation and evolution of binaries, however, in this introduction we would like yet to describe briefly the illustrative case of the Algol system (β Persei) which, at the first sight, might appear to be in contradiction with basic theory of stellar evolution. It was a young Englishman, John Goodricke, who observed that the star called Algol was on the night of November 12, 1782, only about 1/6-times as bright as in the previous night. Goodricke offered several explanations, and one of them, after about another hundred years proved correct: Algol has a companion star which every 69 hours moves (as viewed from Earth) in front of Algol and so obscures it. Today, a number of such systems is known.

If two stars are orbiting around each other, the gravitational potential of the whole system and, correspondingly the gravitational forces acting through the system, may take a complex geometry (see, e.g., Figs. 1.1 and 2.1). Under these circumstances, it may happen that a less massive star evolves more rapidly than a star with a greater mass. This, at first sight, appears to contradict the theory of stellar evolution. In the case of an isolated star, the more massive it is, the faster will evolve and the sooner will die. The resolution of this paradox consists in the detailed understanding of the mass transfer between the individual components of the binary.

The term contact binary star originated from Kuiper [1941], who was the first to attempt to compute how such a structure could exist. He found a discrepancy between the conditions for thermal and hydrostatic equilibrium, which suggested that complex heat and mass exchange must be happening in such systems. These are thought to happen mainly in the common envelope of the two stars.

The term common envelope should not be confused with common envelope evolution in merger astrophysics. This is a fundamentally different concept than

contact binary stars: it is a rather short, evolutionary violent dynamical phase ranging from several months to years, during which the overflow of a Roche lobe of one of the stars causes a common envelope to form around the system. Viscous dragging effects cause this envelope to heat up and when sufficient thermal energy is present, the common envelope gets ejected, taking away a substantial amount of energy and angular momentum, and causing the objects to merge under Hubble time [for a review of the topic, see e.g., Ivanova et al., 2013]. Since the first direct observation of gravitational waves in 2015, merger astrophysics came back to the forefront of research topics, alongside with evolutionary processes in binary physics. The mystery of the origin of merging systems is yet to be fully solved, although it is very probable that many of them had to undergo the common envelope evolution phase. Contact binary configurations, on the other hand, last for nuclear timescales and seem to be stable. A better term for contact binary stars could be "shared envelope", however, due to the nomenclature commonly used in literature, in this thesis, the term common envelope will always mean the envelope of a contact configuration of a binary system stable on large timescales.

From the observational side, instrumental imperfections always lead to significant biases. For instance, many systems are not bright enough to be observed, or in very low mass ratio systems the eclipse depth may be too small to be photometrically detectable (and radial velocity changes too small to be spectroscopically detectable). Nevertheless, Rucinski [1993] provides an interesting overview, especially about systems with low total mass and small contact. Recently, high-quality photometric data from the Kepler mission and significant improvements in light curve fitting techniques have been applied to obtain information about a much broader range of system parameters Kobulnicky et al. [2022].

The Kuiper paradox (see Sec. 1.1) hints at internal mixing mechanisms, such as energy or mass exchange. Indeed, papers as Almeida et al. [2015] found evidence for enhanced internal mixing, due to observing stars in contact configurations with different temperatures than would be expected without mixing. Due to flows generating mixing, it is suggested that magnetic fields could play an important role in contact binary systems. The common presence of sunspots on such systems alongside other observational characteristics would suggest the presence of strong magnetic fields in these systems [see Morgan et al., 1997]. Papers such as Borkovits et al. [2005] even suggest the existence of magnetic cycles.

An interesting relation between the color and orbital period in contact binary systems has been known for a long time [Eggen, 1967]. The most recent observational update on this issue can be found in Jayasinghe et al. [2020]. This relation is thoroughly discussed in section 4.6.1.

Low mass eclipsing contact binary stars are commonly referred to as W UMa stars after the typical W Ursae Majoris. It is estimated that more than 50% of the stars we see are binaries (and this percentage depends on the spectral type). Out of eclipsing contact binaries, about 95% are W UMa type stars. It is not clear how many binary systems undergo the contact phase throughout their lifetime, however, the percentage is thought to be higher for massive stars. With ongoing developments in observational instrumentation, over a million eclipsing binary systems have been found Czavalinga et al. [2022]. As more modern methods such as high-resolution time sequence spectroscopy are applied to binary systems Rucinski [2015], we could have much more detailed information about these mysterious

objects in the near future.

One of the motivations for this thesis was inspired by the results of the recent paper by Jayasinghe et al. [2020]. The authors analyzed a large sample of close binaries based on observations of the ASSASN survey, as well as a number of other archive sources. They noted a clear dichotomy among the contact binaries in the effective temperature versus orbital period space. Intriguingly, the dividing line among these two groups appears to be located near $\simeq 6200$ K. Isolated main sequence stars are known to have a division near this effective temperature, known as the Kraft break, such that massive and hot stars rotate fast and vice versa. This division is traditionally understood using a change of surface layer nature. The cooler stars have deep convective layers that promote magnetic dynamo. Stellar winds carry out the magnetic field and slow down the rotation through the effects called magnetic braking. Massive and hot stars have radiative surface layers and radiatively driven winds without a significant magnetic component. Now the question is whether the contact binary dichotomy is produced by similar phenomena as the Kraft break for isolated stars, or whether something else operates in this case.

Having the motivation in mind, the specific goal of this thesis is to create a new method of determining the structure of contact binary stars. In particular, we combine two standard approaches in stellar modeling to construct simplified models of contact binary systems in the form of one significantly tidally deformed star. The Kippenhahn averaging formalism is the key approach to converting a 3D problem to a 1D approximation. We apply it to the contact binary systems using the Roche equipotentials as the fundamental geometric scaffolding. Obviously, this method cannot capture all complex aspects of the problem, but it could potentially yield insights for further developments of the model.

The thesis is divided into five parts. In the first chapter, a brief history of contact binary system models is reviewed alongside with discussion and observational constraints of different approaches, from Kuiper times to the current state-of-art. In the second chapter, the whole formalism of the newly developed model is outlined, including the correction factors, defined as surface integrals on the equipotentials of the Roche model, as the fundamental parameters. Numerical values of the correction factors, needed to approximately determine the structure of the highly irregularly shaped common envelope system, are computed for a wide range of their defining parameters, the mass ratio q of the binary and the fill-out factor F defining surface of the primary. Our simplified approach allows to determine the structure of the primary component in the binary only, assuming the secondary behaves like a mass point perturber. The third chapter describes the tools and methods used to create stellar models with the MESA code. We briefly comment on the most relevant parts of the code, relegating an interested reader to the original literature. Chapter four contains the principal results of the thesis. Here we apply the formalism and necessary numerical tools developed in the previous two chapters to model the primary component in the short-period binaries (we include both detached and contact configurations). We explore a wide range of important parameters, the mass ratio q, the fill-out factor F, and the mass of the primary M_1. We focus on the determination of the effective temperature and properties of the subsurface layers, as they may be the most relevant for the confrontation with observations. Some of the recent observational

facts about contact binaries are summarized at the end of this chapter, and we try to propose connections with our numerical results. Admittedly, they need justification for using more complex models. Finally, chapter five summarizes approximations made by the model developed in this thesis as well as a few ideas about possible generalizations still within the 1D formulation (before much more complex 2D or 3D approaches are used). We also mention a few more problems in astrophysics, other than contact binaries, where our approach could be possibly applied in the future.

1. Models of contact binary systems

The problem of the structure and evolution of contact binary stars has been subject to research for over 80 years now. During the sixties and seventies, a great effort to construct accurate theoretical models was made. Despite this research continuing until now and a greater abundance of observational data, a clear understanding of the problem is still absent. This chapter serves as a review of historical approaches, models, and fundamental findings constraining possible future solutions.

1.1 Kuiper's paradox

The geometry of a close binary system can be roughly estimated by the well-known Roche potential, which will be further analyzed in Chapter 2. Assuming stellar rotation synchronous with the orbit, Kuiper [1941] proved that in order for a contact configuration to exist the common boundary must lie in between the two critical surfaces of the Roche potential. The synchronous rotation assumption has been thoroughly explored both theoretically and observationally [see, e.g., Meibom et al., 2006, Lurie et al., 2017]. Due to large tidal forces, close systems exhibit both rotational synchronization with orbit and orbital circularization. Traditionally quoted timescales of synchronization and circularization of the orbit were calculated by Zahn [1989]. This configuration with its boundary in the common envelope significantly limits possible stellar parameters, namely the mass-radius relationship. For binaries with masses M_1 and M_2 and radii R_1 and R_2 of the two components, this relation has to have an approximate form

$$(R_1/R_2)_{\text{Roche lobe}} \approx (M_1/M_2)^{0.46}. \tag{1.1}$$

On the other hand, the mass-radius relationship of isolated main sequence stars typically occurring in these configurations is

$$(R_1/R_2)_{\text{main sequence}} \approx (M_1/M_2)^n, \tag{1.2}$$

where the exponent n varies from 0.6 to 1 from upper main sequence towards lower main sequence stars, respectively. Because of this incompatibility, Kuiper argued that contact binary configurations must have mass ratios close to 1 in order to exist. The population of contact binaries, however, has a wide range of mass ratios $q = M_2/M_1$ with extreme cases having $q < 0.1$ [Li et al., 2021]. The mean mass ratio of the population is $q = 0.3$, with a majority of cases being in the range 0.2 to 0.45. Mass ratios close to 1 are fairly rare [e.g., Binnendijk, 1970, Latković et al., 2021, Sun et al., 2020].

1.2 The importance of the common envelope

This discrepancy led Osaki [1965], and particularly Lucy [1968], to propose that the common envelope must play a key role in these configurations. In their

models, the common envelope redistributes energy coming from the two cores and radiates it away. With his model based on continuity at the inner critical surface (coinciding with the contact discontinuity in Fig. 1.1), Lucy confirmed Kuiper's result for radiative envelopes, but showed that the discrepancy does not appear for convective ones. This was an encouraging result since most W UMa stars have later spectral types [Rucinski, 1993]. In Lucy's original models, the convective common envelope had a single specific entropy value due to hydrostatic equilibrium arguments. The value of the specific entropy was then adjusted to be equal to specific entropies of the inner envelopes of the stars underneath. Although Lucy's models worked only in a very small mass range around 2.5 M$_\odot$ and with very specific assumptions (the primary had to be burning through the CNO cycle, whereas the secondary through the proton chain), they provided significant insight into the problem of contact binaries. Lucy's papers were followed by many, expanding the range of masses and other parameters, such as Hazlehurst [1970], Moss and Whelan [1970] or Whelan [1972]. However, none of them reached stable models for the correct variety of observed masses and agreement with observation, such as the color-period relation. Soon after his initial papers, Lucy concluded that his models cannot exist in a stable thermal equilibrium state, but should rather undergo oscillations around a semi-stable configuration. This led to the thermal relaxation oscillation theory of contact binary stars discussed in Section 1.4.

The idea that the common envelope redistributes energy can explain some observational peculiarities, such as why the temperatures of both binary components are the same despite having different masses. However, the mystery of the internal structure of contact binary stars and the precise mechanism for energy redistribution has remained unsolved.

1.3 The contact discontinuity model

Later on Shu, Lubow, and Anderson [Shu et al., 1976] expanded Lucy's model and proposed the so-called contact discontinuity (DSC) model. The motivation for this theory is the assumption that the failure of previous models is due to too strict boundary conditions. This model therefore discarded the assumption of continuity at the inner Roche lobe and replaced it with a possible discontinuity in ϱ and mainly T while keeping pressure continuous. This discontinuity is maintained against thermal diffusion by rapid fluid flow in the innermost sections of the common envelope. The configuration can be seen for the convective case in Fig. 1.1. Effectively, these assumptions lead to the specific entropy of the envelope possibly having a different value than the interior of one of the stars as opposed to Lucy's model. This additional "freedom" (which can be quantified for example by the temperature discontinuity ΔT) allowed more advanced static models. In their papers, Shu, Lubow, and Anderson calculated models for both radiative and convective envelopes as opposed to only convective envelope models of Lucy. Some pointed out that in order for an infinitesimal contact discontinuity to exist, mainly a discontinuity in luminosities, infinite flows would be required. This problem is occasionally referred to as Lucy's paradox [Shu, 1980].

Because of this, Lubow and Shu [1979] concluded that in order for a DSC model to function, the contact discontinuity has to be a layer of temperature
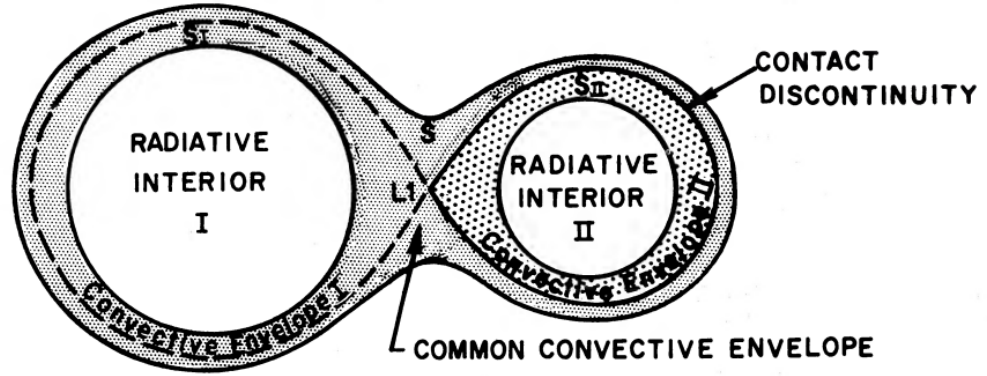
Figure 1.1: Illustration of the contact discontinuity model the case of convective envelopes, adapted from Shu et al. [1976]. The contact discontinuity is highlighted along with two separate entropy value regions.

inversion of some finite thickness. Several works tried to construct heat engine models which would support such a structure and prove its stability [Shu et al., 1980, Smith et al., 1980]. The controversial proposition of a temperature inversion layer led to many attacks of the model. Ultimately, they were mostly proven to not be possible without violating the second law of thermodynamics [Hazlehurst, 1993].

Eggleton [1982] argued that even the primary motivation for this model is incorrect and that rather than constructing an artificial static model, a better way of the liberation of the boundary condition is taking the mass of both stars together and then mass transfer between them as an additional degree of freedom.

1.4 Thermal relaxation oscillation theory models

As was mentioned in Section 1.2, after failures of static models, Lucy argued that due to instabilities his model will undergo some oscillatory cycles. These models proposed by Lucy [1976], and expanded by Robertson and Eggleton [1977] and Kähler [1986], are referred to as the Thermal relaxation oscillation (TRO) models. On a qualitative level, the cyclic nature of the expansion of Lucy's theory can be summarized in the following steps:

- An initial configuration similar to Lucy's model is established, where the common envelope has the same specific entropy as the inner envelopes under the inner critical surface.

- Due to this configuration the secondary expands and mass transfer to the primary begins. Due to this mass transfer, the mass ratio of the system shifts, and eventually the secondary does not fill its Roche lobe. The system becomes detached.

- After losing contact the secondary naturally shrink to its main sequence size. The primary expands to its natural isolated state, but afterwards it starts to fill its Roche lobe. Due to this filling mass transfer starts, which causes the orbit to shrink, and contact is established again.

- While establishing contact, the envelope of the primary has larger entropy than the secondary and, therefore, flows around the secondary arise and the common envelope forms. This creates the contact discontinuity. This configuration is maintained on the thermal timescale, on which is heats up the upper parts of the secondary. Throughout this heating the original configuration is established and the cycle begins anew.

Alongside the contact discontinuity model, this was the leading theory of contact binaries in the 70s and the discussions were lively [Shu, 1980]. The two theories –DSC and TRO– do not necessarily directly contradict each other - the equilibrium that the TRO model oscillates around could be precisely the contact discontinuity model. The difference in opinions boils down to the stability of DSC. The TRO school proposed that it can only last on the thermal timescale, while DSC proponents constructed mechanisms throughout which the discontinuity could be maintained on the nuclear timescale.

The TRO model seemed to solve some stability and consistency problems of the contact discontinuity model, and mainly managed to be in accordance with the observed mass distributions and even the period - color relation. The major downside was in its failure to reproduce observed light curves. This discrepancy naturally arises due to the phase without contact where the temperatures of the two components differ by a larger value than observations would suggest, and led Hazlehurst [2001] to denounce the TRO model.

A later review of this assessment, however, points out that this discrepancy may have been cause by insufficient observational data [Paczyński et al., 2006]. This 2006 survey found enough close binaries in the semi-detached configuration of the TRO cycle. With these new observations, TRO type theories are not fully off the table yet.

1.5 Later models of Kähler

From the end of the 70s the problem of the structure of contact binaries had lost its place at the forefront of stellar research. This was the fate of many astrophysical problems until the 90s due to the lack of observational data. In his review, Eggleton attributed this shift either to the fact that possible models have been developed to a large extent, or, on the other hand, that state of the art models were "stuck" not being able to fully reconstruct observed light curves and system parameters.

Nevertheless, several new models and semi-analytical approaches appeared, namely a series of papers by Kähler [2002b] and Kähler [2002a]. Kähler attributed the lack of success of previous models to overly strict assumptions. He therefore constructed models based on the weakest possible assumptions for the stellar equations and boundaries possible. Despite this approach, further in his models he employed some assumptions that are arguably artificial. These include the assumption that energy sources and sinks appear only in outer layers and in the same mass percentage in both stars. He also used specific formulas for mass transfer rates which may not have to be valid. He found two solutions that either stay in contact due to mass transfer when it is possible, or in most cases have a cycle similar to the TRO theory, with the no-contact phase fairly short.

Cumulatively, the failure of these models was in insufficient contact: observed W UMa systems have much more greater contact, which was not theoretically reproduced.

In his last paper on the topic of contact binary stars, Kähler [2004] proposes some elegant possible solutions to uncertainties of some previous models, namely the inversion layer mentioned in Section 1.3. These models rely on deviations of the system from the Roche potential due to additional internal circulatory flows, which enable thermal equilibrium. Additional forces from these flows can, for example, aid with explaining a pressure inversion zone needed for the contact discontinuity model. This is done by circulation luminosity - luminosity carried by circulation currents through level surfaces. The corresponding decrease in the temperature gradient is able to sustain a thermal equilibrium model similar to the DSC model. The effects of these flows given by certain circulation functions still contain free parameters such as the energy transport efficiency, which are somewhat arbitrary, as well as the velocity field of the flow itself.

From the observational side, Rucinski [2015] and several others used high-frequency time-resolved spectroscopy methods to observe line broadening corresponding to large flows in common envelope binaries. A significant structure of strong equatorial flow rotating around the binary faster than the rest of the system was observed, similar to Kählers flow prescriptions. There is some observational uncertainty since this flow could also be attributed to an external disk-like structure. Rucinsky also observed strong movements that were significantly non-uniform, with irregular spots traveling with different velocities, which could point to significant convection in the common envelope in general.

1.6 Newer models

Since then, not many more papers studying the structure of contact binary stars appeared. Li et al. [2004] studied models with different vertical positions of energy transfer in the common envelope. They found that these modifications significantly affect the structure and evolution of the system. Comparing simulations with observations, they concluded that in W type systems, energy transfer may occur in the outermost layers of the common envelope, whereas A type systems could have energy transfer in deeper levels.

Some newer papers, such as Stępień [2009], continue in the steps of Kähler with more and more complex modeling of flows. As more precise observational constraints on flow structures will be available, papers like these may become more common.

Stepien [2005] studied the evolution of contact systems and proposed a revolutionary evolutionary approach, where contact binaries of the W UMa type are old objects past a mass exchange phase with a reversed mass ratio. The proposed evolutionary paths start with angular momentum loss due to magnetized wind. This evolution has a similar timescale as main sequence evolution of typical stars in these configurations, which would explain the old age of the components. After Roche lobe overflow, significant mass transfer until the mass ratio inverts.

An article from this year, Fabry et al. [2022], proved that the problem of the structure of contact binary stars might be revisited in the following years. This is the first paper in a series that should deal with many aspects of the structure

of contact binary systems. As the model from their article has close similarities to the new approach in this thesis, it will be thoroughly discussed in the next chapters.

Advancements in computer capability could even allow full 3D magnetohydrodynamic models to be possible in the future, which might be needed for the full understanding of the problem of the structure of contact binary systems.

2. Model set-up and correction factors of the Roche geometry

In this thesis, we developed a new approach, that has certain similarities to the contact discontinuity model. It also aims for a stationary description of a common envelope configuration, although it does not thoroughly model complex flows in the common envelope needed. The fundamentals consist in the application of an elegant approach to the reduction of a three-dimensional problem to one dimension, assuming the equipotentials are topologically equivalent to spheres. The formalism is further applied to a standard binary system model - the Roche potential - via *correction factors*. In this chapter, the mathematical formalism is introduced and the results of numerical calculations of correction factors are presented.

2.1 Modified stellar structure equations

The origins of the employed approach were introduced by Faulkner et al. [1968], who divided rotating stars into several zones ranging from fully spherical in the center to significantly deformed in the outer layers. They solved the stellar structure equations in these zones separately, accounting for the correction factors due to the rotationally-imposed deviation from spherical geometry. Two years later Kippenhahn and Thomas [1970] fully developed this mathematical formalism into its differential form, where the stellar structure equations are solved for equipotential shells with appropriate correction factors.

Consider a general conservative potential Ψ, where equipotential surfaces $\Psi = C$ are topologically equivalent to spheres. For these equipotentials, we denote average values of any scalar quantity f by averaging over the surface

$$\langle f \rangle = \frac{1}{S_\Psi} \int_{\Psi=C} f \, d\sigma, \tag{2.1}$$

where the integration is taken over the equipotential surface, and $S_\Psi = \int_{\Psi=C} d\sigma$ is its total area. We also denote the volume enclosed by the equipotential as V_Ψ and in the spherical analogy define the equivalent radius as $r_\Psi = \sqrt[3]{\frac{3V_\Psi}{4\pi}}$. Finally, in the relevant case of gravitational potential, we denote the mass enclosed by the equipotential as M_Ψ.

A fundamental assumption of the model is "shellularity", i.e. the thermodynamic parameters (such as the pressure or temperature) are constant over the equipotential surfaces, an assumption equivalent to baroclinicity. This is the case in hydrostatic equilibrium, however, such a configuration cannot exist in radiative equilibrium [see Von Zeipel, 1924]. Nevertheless, strong horizontal flows should ensure solid isobar rotation and approximately keep the shellular approximation valid [Zahn, 1992].

Since density ρ is constant over equipotentials, the Lagrangian mass conservation equation has the same form as in the spherical case

$$\frac{\mathrm{d}r_\Psi}{\mathrm{d}M_\Psi} = \frac{1}{4\pi r_\Psi^2 \rho}. \tag{2.2}$$

Using the standard definition notation for effective gravity g (note that aside from the gravitational part, the potential Ψ may also contain contributions from other effects, such as the centripetal, non-inertial forces in the Roche model)

$$g = \|\nabla\Psi\| = \frac{d\Psi}{dn},$$

(2.3)

we can write the potential differential as

$$d\Psi = \left(\frac{dV_\Psi}{d\Psi}\right)^{-1} dV_\Psi = \left(\frac{dV_\Psi}{d\Psi}\right)^{-1} \frac{dM_\Psi}{\varrho} = \frac{dM_\Psi}{g^{-1}S_\Psi\varrho}.$$

(2.4)

Combining this relation and Eq. (2.2) with the general form of hydrostatic equilibrium $\partial P/\partial\Psi = -\rho$, one obtains a corrected equilibrium equation

$$\frac{\partial P}{\partial M_\Psi} = -\frac{GM_\Psi}{4\pi r_\Psi{}^4}f_p,$$

(2.5)

where we define a correction factor f_p as

$$f_p = \frac{4\pi r_\Psi{}^4}{GM_\Psi S_\Psi} \frac{1}{\langle g^{-1}\rangle}.$$

(2.6)

A similar treatment can be applied to the energy conservation equation. For zones with radiative energy transfer, the energy flux is proportional to the local effective gravity

$$F = -\frac{4acT^3}{3\kappa\varrho}\frac{dT}{dn} = -\frac{4acT^3}{3\kappa\varrho}g\frac{dT}{d\Psi}.$$

(2.7)

The total equipotential luminosity is obtained by integrating over the shell. By using Eq. (2.3)

$$L_\Psi = \int_\Psi F \, d\sigma = -\frac{4\pi acT^3}{3\kappa}\left\langle g^{-1}\right\rangle \langle g\rangle S_\Psi^2 \frac{dT}{dM_\Psi}.$$

(2.8)

The modified Lagrangian form of the radiative transport equation is therefore

$$\frac{dT}{dM_\Psi} = -\frac{3\kappa L_\Psi}{64\pi^2 acT^3 r_\Psi^4}f_T,$$

(2.9)

where the second correction factor f_T is introduced as

$$f_T = \left(\frac{4\pi r_\Psi^2}{S_\Psi}\right)^2 \frac{1}{\langle g\rangle\langle g^{-1}\rangle}.$$

(2.10)

In a more standard form, combining Eqs. (2.5) and (2.9), the temperature equation can be written as

$$\frac{\partial\ln T}{\partial\ln P} = \frac{3\kappa L_\Psi}{16\pi acGM_\Psi}\frac{P}{T^4}\frac{f_T}{f_p} \equiv \nabla_{\mathrm{rad}}\frac{f_T}{f_p},$$

(2.11)

in which the traditional definition of the radiative gradient ∇_{rad} has been introduced.

Accounting now for the possibility that in some stellar layers the energy transport by convection may dominate the radiative transport, locally tested using the Schwarzschild criterion for convection, the general temperature equation becomes

$$\frac{\partial \ln T}{\partial \ln P} = \min \left[\nabla_{\mathrm{ad}}, \nabla_{\mathrm{rad}} \frac{f_T}{f_p} \right], \tag{2.12}$$

where ∇_{ad} is the appropriate convective gradient (we assume adiabatic approximation, thence the subscript ad). The full system of stellar equations is closed by an equation of state, which is discussed in section 3.3, and an equation for luminosity gain due to nuclear energy

$$\frac{\mathrm{d}L_\Psi}{\mathrm{d}M_\Psi} = \epsilon, \tag{2.13}$$

where ϵ is the energy generation rate.

For isolated and non-rotating stars, spherical geometry may be assumed, and both correction factors are equal to unity. This leads to the standard stellar structure equations. In general, f_p tends to deviate from 1 more than f_T. As a result, sometimes a crude approximation in which only f_p is taken into account has been employed [e.g., Meyer-Hofmeister, 1972].

This original formalism was extended by Endal and Sofia [1976] to model the structure of the rotating stars. In this case, angular momentum arguments are used to determine the shape of the potential, from which the correction factors are calculated. Kippenhahn's original set-up was used in many works describing the effects of stellar rotation [Smith, 1973, Basu et al., 2000, Fujimoto, 1993], as well as stellar winds [Mendes et al., 1999]. An extension for shell-like rotation was performed by Meynet and Maeder [1997], and further used in many studies [e.g., Potter et al., 2012, Yang and Bi, 2006].

The correction-factor formalism is also implemented in widely used numerical packages for stellar astrophysics, such as the YREC code [Pinsonneault et al., 1989], in order to model the effects of rotation. More recently, it has also been made part of the MESA stellar code, also used in this thesis, by Paxton et al. [2019]. More details about MESA can be found in Chapter 3.

2.2 Roche geometry application

The general formalism described in the previous section was originally intended for rotating stars, however, contact binary systems and tidally deformed stars in general offer an interesting application too. A very useful approximate model for studying binary systems is the Roche potential [e.g., Roche, 1873, Eggleton, 2006]. This is the potential of two point masses M_1 and M_2 in a stationary configuration orbiting around each other and separated by a constant distance d (the period P of their revolution in the inertial space is a function of the total mass $M_1 + M_2$ and d through the third Kepler's law). If we choose a coordinate system centered in the primary having mass M_1 and with the x axis directed towards the secondary at the scaled unitary distance from the primary, the Roche potential Ψ_{Roche} can be written in the co-rotating frame as

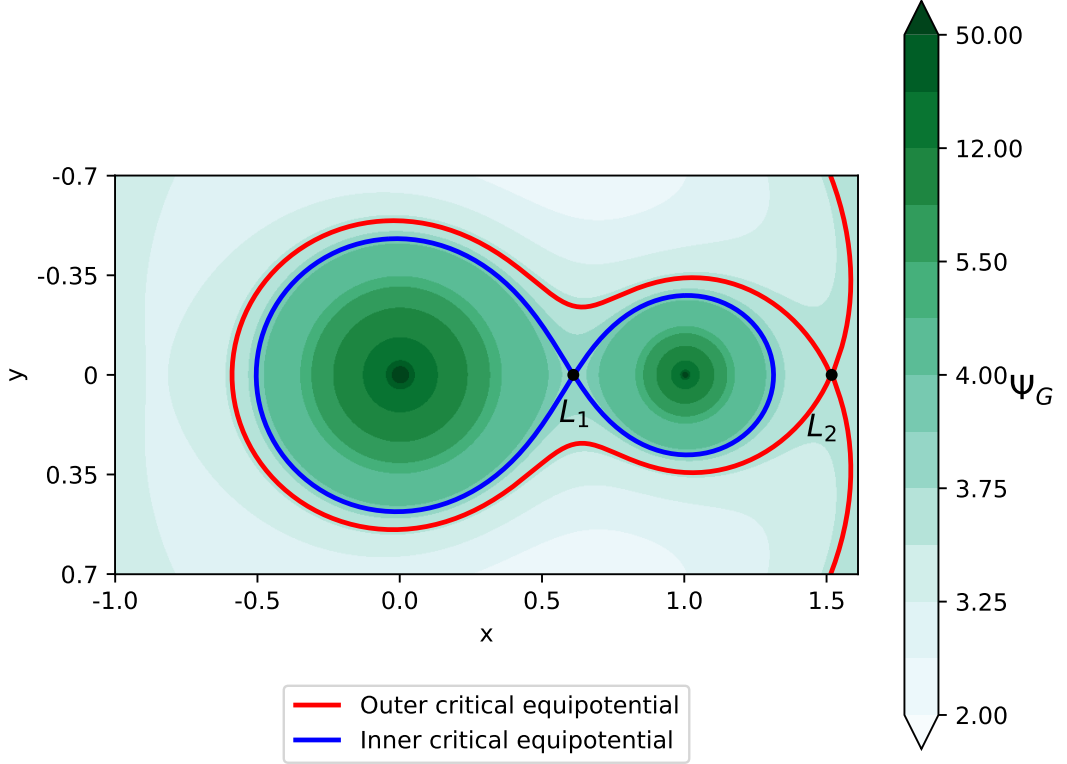$$\Psi_{\mathrm{Roche}}(x,y,z) = -\frac{G\,(M_1 + M_2)}{2d}\Psi(x,y,z), \tag{2.14}$$

Figure 2.1: Illustration of the geometrized Roche potential for mass ratio $q = 1/3$. The two critical equipotentials, inner (blue) and outer (red) are shown, as well as the two Lagrangian points L_1 and L_2 defining them.

where

$$\Psi(x, y, z) = \frac{2}{1+q} \frac{1}{(x^2 + y^2 + z^2)^{1/2}}$$
$$+ \frac{2q}{1+q} \frac{1}{[(x-1)^2 + y^2 + z^2]^{1/2}} + \left(x - \frac{q}{1+q}\right)^2 + y^2 \tag{2.15}$$

is the geometrized (non-dimensional) Roche potential, and q is the mass ratio of the system

$$q = \frac{M_2}{M_1}. \tag{2.16}$$

Note that we might choose $M_2 \leq M_1$, therefore $q \in (0, 1]$, without loss of generality, since a simple interchange of indices 1 and 2 describes the opposite situation. However, we shall not impose any constraint on masses, thus $q > 0$ only. This apparent redundancy allows us to locate the origin of the reference system at the center of the heavier component ($q < 1$) or lighter component ($q > 1$) in the binary. In passing, we also note that equipotentials $\Psi(x, y, z) = C$, with C diverging to infinity, become asymptotically spherical surfaces around the origin with radius $\simeq 2/(1+q)/C$. At that limit, the stellar structure converges to that of an isolated object with correction factors close to unity.

The parameter q fully defines the geometry of the potential, whereas the additional physical parameters - the total mass and separation distance - specify

only the scaling of the values of this potential. This geometry has five critical points, all of which are saddle points in 3D space, commonly referred to as Lagrange points (see Fig. 2.1). Related to them are several important equipotentials of the model, commonly referred to as the critical equipotentials. The point L_1 is located in between the components on the equipotential defining the two potential lobes (the Roche lobes), which represent terminal configurations in which the stars can exist as individual objects. This equipotential surface is often called the inner critical equipotential. Above this surface, the equipotentials start to wrap around both stars, creating a common envelope. Point L_2 defines the outer critical surface. Equipotentials above the second Lagrangian point are already open at this point, meaning that they are topologically not spheres. In this geometry, stars gradually fill equipotential surfaces. Overfilling the outer critical equipotential results in a rapid mass loss through the outer Lagrange point L_2 (Kuiper [1941],Shu et al. [1979]). Since we are examining stationary contact configurations in thermal equilibrium, the range of this study will be limited to systems where there is no overflow of the outer critical equipotential and therefore no mass loss from the whole system occurs.

The Kippenhahn averaging formalism is valid for any equipotentials topologically equivalent to spheres. If the separation of the stars in the binary is large enough for the primary not to overflow the corresponding Roche lobe in the configuration, the topology is not a problem and we get a star with a teardrop-like shape. However, Kippenhahn's requirement is not satisfied for contact binary systems, where this would be the case only outwards of the inner critical equipotential. It is, however, possible to use an approximation, where we model the secondary as a point mass which tidally deforms the primary. The idea works as follows.

If the stars are close enough for mass to overflow the primary Roche lobe, we approximate the second star as a point mass in a "shell" with the same volume as the volume of the secondary Roche lobe. The result is a single deformed star with a "hole", in which simply the equipotential following that of the Roche lobe covers both stars in a contact configuration. This step creates a significant jump in the equipotential parameters such as the surface area S_Ψ as well as enclosed mass M_Ψ. In a realistic model, the presence of the secondary should also contribute with its luminosity, resulting in a jump in L_Ψ. This approach would, however, require modelling of the secondary component as well. Instead, here we collapse the secondary into the point and account just for its tidal effect on the primary. Our only focus is modelling the structure of the primary. As a result, we adopt three approximations at the point, when the layers exceed the inner critical Roche equipotential; (i) we subtract the volume of the secondary Roche lobe from the computed volume V_Ψ of the contact equipotentials, (ii) the mass of the secondary is accounted for in the equipotential geometry (and thus also local variables related to local acceleration such as g or g^{-1}), but not included in the mass variable M_Ψ in the equations determining the primary structure (Sec. 2.1), and (iii) we neglect the contribution of the secondary to the luminosity budget. The former conditions (i) and (ii) imply the radius r_Ψ and mass M_Ψ are continuous over the inner critical equipotential (describing thus in a single object). The last condition (iii) means that our solution is less accurate and justified when q becomes close to unity. Figure 2.2 provides a schematic diagram of a contact configuration and our approach described above.
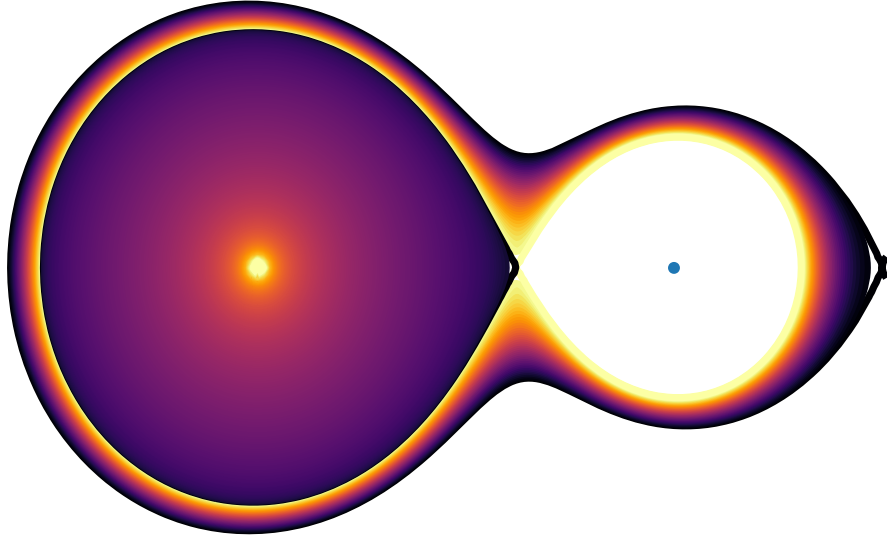
Figure 2.2: Schematic description of the geometry of the newly developed stellar model. The secondary is modeled a point mass which tidally distorts the primary. Due to this tidal distortion, the equipotentials of the primary eventually "overflow" the secondary (this occurs when they reach the L_1 point) and form a common envelope.

Before we discuss our results for the correction factors determined in the strict Roche model, with the two point-mass sources, we pay a short comment on an approximate way how they are implemented in the MESA code. When using this software package to construct a standard 1D stellar model, one has to calculate the f_p and f_T correction factors for all cells in the star. In order to preserve basics of the Roche geometry, but go a step beyond the point-mass model, the correction factors for every cell are calculated from the Roche potential with the mass ratio q set by the mass enclosed by the current shell of the primary – this is to be used as M_1 – to the conserved total mass of the secondary, still modelled as the point mass M_2. This effectively means that outer shells do not tidally affect the distortion of the inner ones as usual. But there are two aspects of the approximation. First, the mass M_1 is dynamically added as the model is constructed from inside out. Second, the outer potential shells may, if they were modeled rigorously, deviate from the simple Roche model prediction by the effect of the underneath mass spread over a certain volume. Obviously, a combination of the two effects amplifies toward the outer stellar layers. Initially, the innermost equipotentials of the primary star have small enclosed mass, usually smaller than the secondary point mass, and they are still nearly spherical. After some point, where the equipotential mass is equal or greater than the secondary mass and the equipotential already deformed, the approximation becomes less precise. Still, the generic strong mass concentration towards the center in stellar models roughly justifies our approach.

2.3 Correction factor calculations

In order to obtain correction factors for stellar equations, accurate integrations of the Roche potential were essential. Integration tables of equipotential parameters have been previously calculated by Mochnacki [1984] for each star in the binary system separately, where the separation was chosen as a vertical plane slicing through the L_1 point. The tables are unfortunately not dense enough for the usage of the aforementioned method in stellar codes - interpolation would not yield precise enough values. Wilson [1978] calculated values even for the common envelope, but did not publish his tables. In this thesis, the range of integrated equipotentials has been greatly expanded as well as the range of mass ratios of the systems.

Integrations were computed for the dimensionless Roche potential from Eq. (2.15). In order to calculate correction factors for all cells in stellar simulations, a broad parameter space had to be explored. Mass ratios were sampled using a dense grid of equal steps in $\log q$ in the range $-6 \leq \log q \leq 6$. For a fixed mass ratio, there are many ways to parameterize the chosen equipotential $\Psi(x, y, z) = C$, essentially mapping the semi-open interval of C values in $[C_2, \infty)$ to a more suitable finite interval of values of a new parameter. Older literature tend to use the "fill-out factor" defined as

$$F(C) = \begin{cases} C_1/C, & (C \geq C_1) \\ (C_1 - C)/(C_1 - C_2) + 1, & (C_1 \geq C \geq C_2) \end{cases} \tag{2.17}$$

where C_1 and C_2 are values of the critical equipotentials connecting to L_1 point (the Roche lobe) and the outer critical surface passing through outer Lagrange point L_2. Note that the definition interval $C \geq C_2$ of the interest maps to the $(0, 2]$ interval for F. The important values are (i) $F \to 0$ for $C \to \infty$, for which the equipotentials become tiny spheres about the origin, (ii) $F = 1$ for the inner critical surface connected to L_1 and having $C = C_1$, and (iii) $F = 2$ for the outer critical surface connected to L_2 and having $C = C_2$.

Some newer papers, such as Fabry et al. [2022], parametrize equipotentials based on their equivalent radius in the units of the Roche lobe radius, thus $a = r_\Psi/r_{\text{Roche}}$; here $r_{\text{Roche}} = r_\Psi$ for a specific value $\Psi = C_1$. This is suitable for further direct use in standard stellar codes. However, in the case of this thesis we keep using the parametrization via the fill-out factor, since it conveniently covers the possible parameter space of studied equipotentials.

Various quantities were computed for a full range of fill-out factors F using 200 equal-size steps from 0 to 2. An additional table with an improved precision was computed for the range of parameters most often seen among the stellar common envelope models (see Chapter 3). This additional table only covered mass ratios $-2 \leq \log q \leq 2$ with twice smaller step in fill-out factor F and quadruple density in mass ratios.

2.3.1 Integration methods and results

The Roche geometry has two plane symmetries, both containing the axis connecting the two stars, namely $y = 0$ and $z = 0$. This is because the y and z coordinates appear in Ψ only through quadratic terms y^2 and z^2 (note, however, that the

equipotentials are not rotationally symmetric about x). When evaluating surface integrals over the equipotentials, such as in Eq. (2.1), it is therefore sufficient to integrate over one "quadrant" only. Since the common envelope equipotentials are not convex volumes, it was not possible to integrate via spherical coordinates, which would for nearly spherical bodies yield more precise integrations, cylindrical coordinates proved to be the simplest choice due to the existence of a natural principal axis of the problem [this choice has also been used in the previous studies, e.g., Mochnacki, 1984]. Let us therefore choose this cylindrical coordinate system denoting the coordinate along the axis x, the radius from the axis ρ, and the polar angle ϕ.

Given the definition of the f_p and f_T factors in Eqs. (2.6) and (2.10), the following integrals of the potential from Eq. (2.15) were needed [the formula for V_Ψ correcting a small typo in Mochnacki, 1984]

$$
\begin{aligned}
V_\Psi &= \frac{1}{2} \int_\Psi \rho^2(x,\phi)\, dx d\phi, \\
S_\Psi &= \int_\Psi s(\phi,x)\, dx d\phi, \\
\langle g \rangle &= \frac{1}{S_\Psi} \int_\Psi g(\phi,x) s(\phi,x)\, dx d\phi, \\
\langle g^{-1} \rangle &= \frac{1}{S_\Psi} \int_\Psi g^{-1}(\phi,x) s(\phi,x)\, dx d\phi,
\end{aligned}
\tag{2.18}
$$

where $g(\phi,x)$ is the gradient of the potential (Eq. 2.3) and $d\sigma = s(\phi,x)\, dx d\phi$ is the surface element with

$$
s(\phi,x) = -\frac{g(\phi,x)\rho(\phi,x)}{\Psi_{,y} \sin\phi + \Psi_{,z} \cos\phi},
\tag{2.19}
$$

where $\Psi_{,y}$ and $\Psi_{,z}$ are partial derivatives of the potential in the original Cartesian coordinates centered at the chosen primary, as in Eqs. (2.14) and (2.15). When calculating the radius (distance) $\rho(\phi,x)$ from the axis to the equipotential, the equation $\Psi(x,\rho,\phi) = C$ has always at least two solutions, except for the Lagrange points. It was therefore needed to ensure the convergence to the equipotential closest to the x axis by writing specific root finding methods for the Roche problem. The basis of this method is starting in a point that is always nearer to the axis and gradually decreasing step-sizes as one moves outward. A similar approach with a different analytical guess was employed to calculate the x-axis integration bounds, inspired by Kopal [1959]. Some more technical details and explicit formulas are given in the Appendix A.

Note that the f_p factor depends also on the mass M_Ψ enclosed by the equipotential. Due to the normalization in Eq. (2.15), where the combined mass is scaled to 1, the dimensionless mass of the primary is $1/(1+q)$, and the secondary $q/(1+q)$. Because in the Roche model the stars have their mass concentrated in their center (as a good approximation of the reality), the formally integral-defined mass M_Ψ over potential surfaces becomes trivial: (i) up to the critical equipotential reaching the L_1 point (the Roche lobe) we have $M_\Psi = 1/(1+q)$, (ii) whereas for common envelope equipotentials this factor is equal to 1. As a result, parameters defined in Eq. (2.18) constitute a complete set needed for f_p and f_T computation.

The actual integration was performed using a cubic interpolation scheme with 600 divisions in the x direction and 100 divisions in ϕ (these values were chosen

through convergence tests to reach the desired precision). The range of x-values, namely $(x_{\min}, x_{\max})$, is determined for a given equipotential C by numerically solving $\Psi(x, 0, 0) = C$, while the range of the polar angle ϕ is always $(0, \pi/2)$. In all integrals, the step size was greatly reduced at the last 10% limits of the x-interval. In integrals involving the surface element $s(\phi, x)$, the value of the denominator in the surface element in this particular coordinate description may approach zero at the end of the x interval, i.e., when $x \to x_{\min}$ or $x \to x_{\max}$. The reason for this behavior is intuitively clear and has to do with the choice of (x, ϕ) to be the coordinates delimiting the infinitesimal surface element $d\sigma = s(\phi, x)\, dx d\phi$. This choice becomes singular when the equipotential crosses the x-axis, and the formal $dx \to 0$ limit must be compensated by the divergence of $s(\phi, x)$, causing a loss in the accuracy of numerical evaluation. For this reason, the integral evaluation using cylindrical coordinates was restricted to the x values for which $s(\phi, x)$ was smaller than a chosen limit, and the integration over the remaining "caps" of the equipotential was completed in spherical coordinates. Some more details can be found in Appendix A. A customization to an adaptive quadrature using the QUADPACK library was used to compute the actual parts of the integrations Piessens et al. [2012]. After computing these parameters, correction factors are determined from Eqs. (2.6) and (2.10).

In Fig. 2.3 a 2D representation of several relevant integral parameters is shown as a function of the fill-out factor F for a specific mass ratio of $q = 0.5$. Under the inner critical potential (i.e., $F < 1$), the available data points from Mochnacki [1984] are plotted for comparison. The important section to notice is naturally the area around $F = 1$ - the inner critical surface of the Roche potential. Since the second star is added at this equipotential, discontinuities in the equipotential parameters appear. The jumps in the equivalent radius and surface area are directly related to the volume and surface of the second star. In fact, this may be used to check the precision of the integrated values. We verified that for all calculated mass ratios the jump was roughly equal to the expected value.

Figures 2.5 and 2.4 show 3D plots of the computed correction factors f_p and f_T, here as a function of their two parameters: the fill-out factor F and the mass ratio q. All values are bounded in roughly the interval $[0.4, 1.5]$. One can easily verify two expected properties of these results. First, at the limit $F \to 0$ we obtain both $f_p \to 1$ and $f_T \to 1$ for all q values. This is the limit of equipotentials becoming tiny spheres about the origin (Sec. 2.2), thus the stellar structure converging to that of an isolated star. Second, both correction factors f_p and f_T are for $F > 1$ symmetric in $\log q$ measure about the value $\log q = 0$. This symmetry transformation corresponds to mapping q to $1/q$, and thus simply swapping the role of the primary and secondary component in a binary having the same mass ratio. Both configurations then have identical equipotentials with $C \in (C_1, C_2)$, namely those overlapping both stars in between L_1 and L_2 points.

In order to obtain the corresponding physical quantities from their computed non-dimensional integral versions, we recall the scaling of length by d and mass
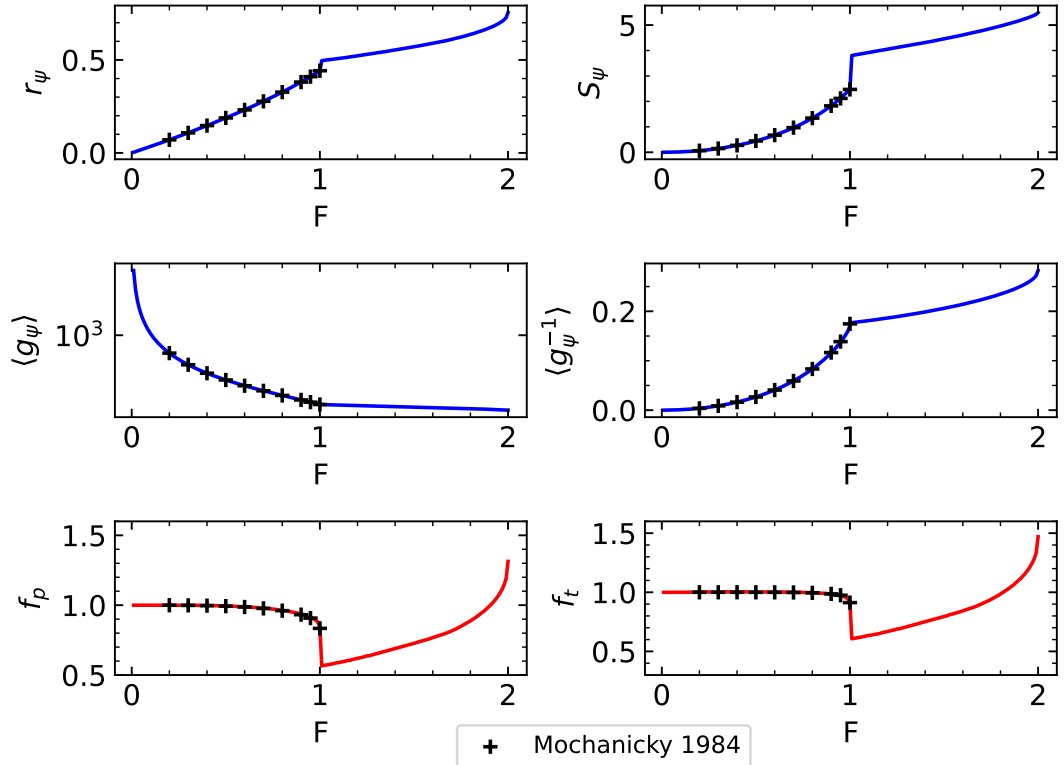
Figure 2.3: Example of various dimensionless quantities computed by the integrals over equipotential (the mass ratio fixed to $q = 0.5$): from top to bottom and left to right the equivalent radius, surface area, average gravity, average inverse gravity, and the correction factors f_p and f_T all given as a function of the fill-out factor F. Crosses denote values calculated by Mochnacki [1984] in intervals of F, where comparison can be made.

by $(M_1 + M_2)$. As a result [see also Mochnacki, 1984]

$$
\begin{aligned}
\mathcal{R} &= d\, r_\Psi, \\
\mathcal{S} &= d^2\, S_\Psi, \\
\mathcal{G} &= \frac{G\,(M_1 + M_2)}{2d^2}\, \langle g \rangle, \\
\mathcal{G}^{-1} &= \frac{2d^2}{G\,(M_1 + M_2)}\, \langle g^{-1} \rangle.
\end{aligned}
\tag{2.20}
$$

2.4 Comparison with the work of Fabry, Marchant and Sana (2022)

During the late phase of this research, a similar approach was independently published by Fabry et al. [2022]. Despite this coincidence, and the fact that both works aim to be a proof of concept of the correction factor formalism using the Roche geometry, there are fundamental differences in our application of this method. Firstly, the focus of Fabry et al. [2022] is on the surface temperature variability and the effects of rotation in both binary systems and single rotating

Figure 2.4: f_T correction factor as a function of the fill-out factor F and mass ratio q (in log scale). Note the two properties discussed in the main text: (i) $f_T \to 1$ for $F \to 0$, and (ii) symmetry of f_T about $\log q = 0$ for $F > 1$.
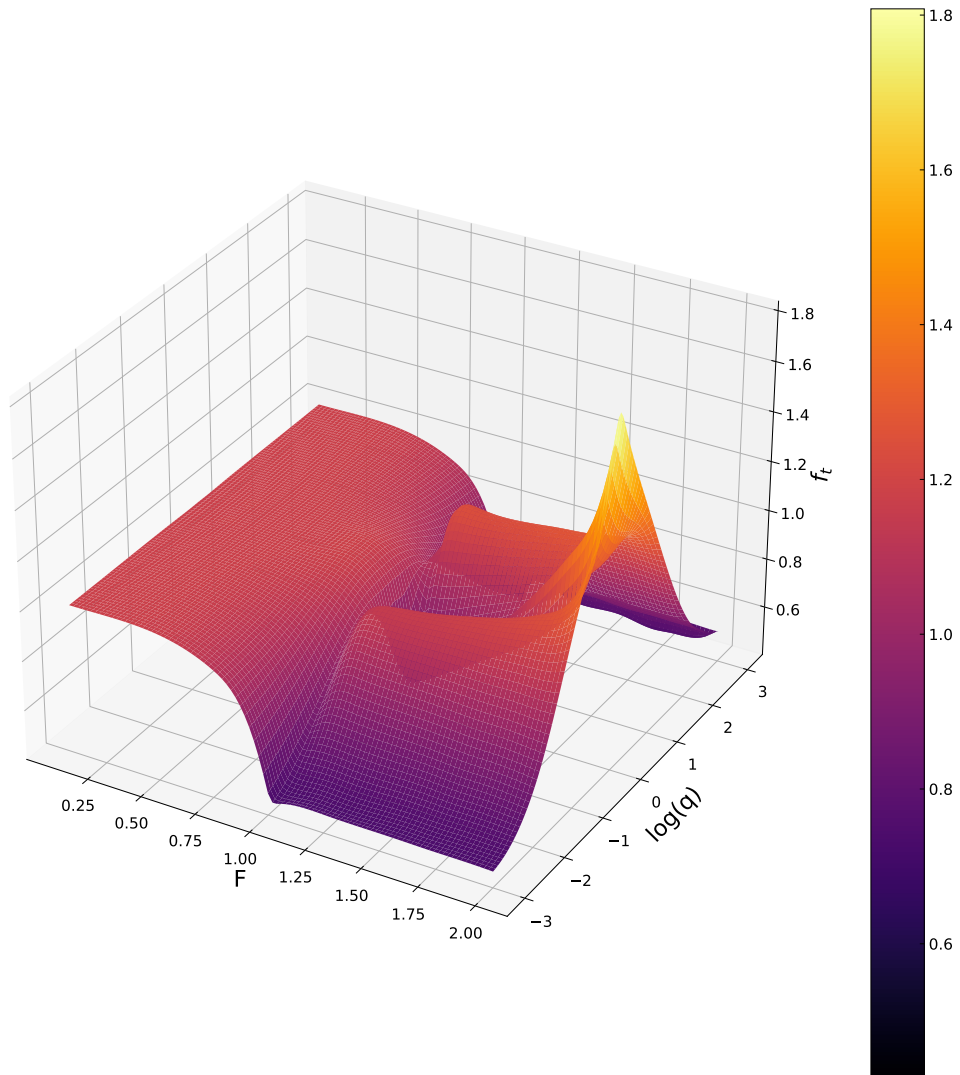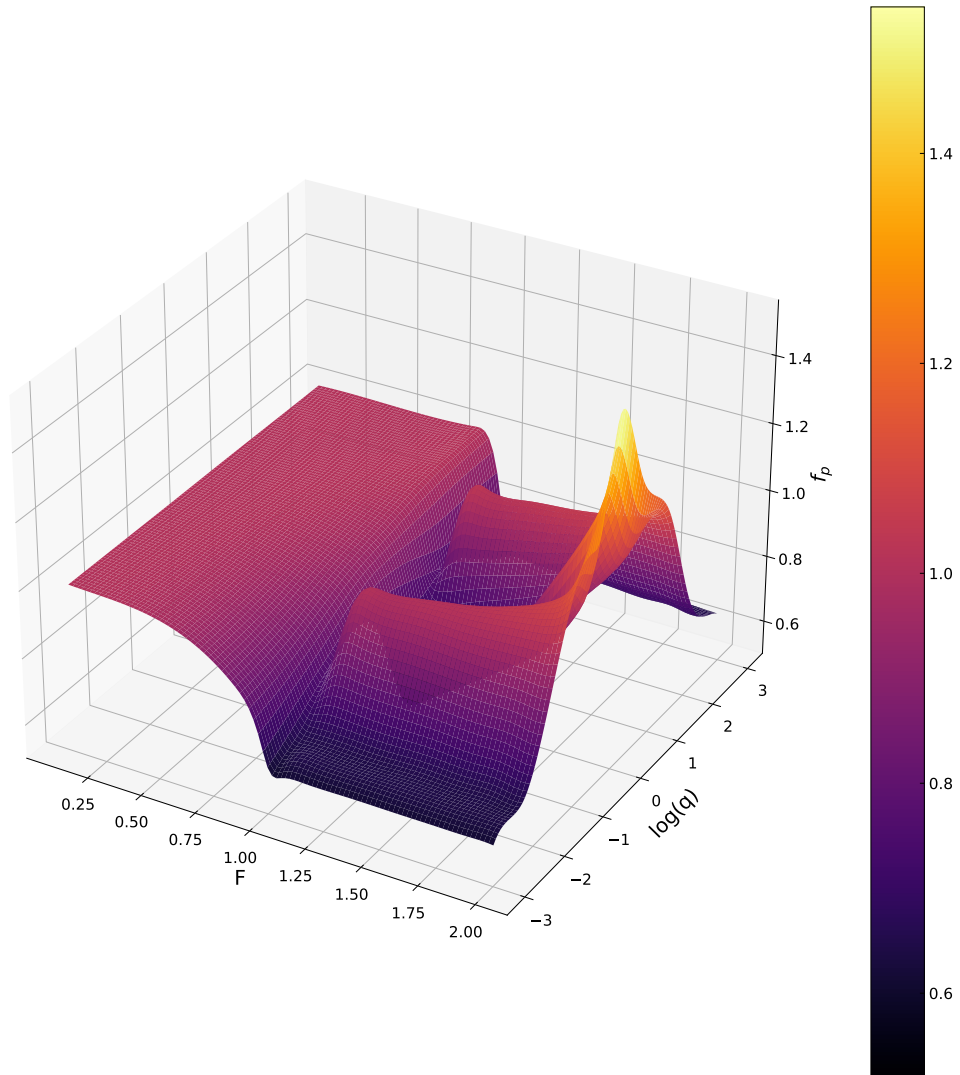
Figure 2.5: f_p correction factor as a function of the fill-out factor F and mass ratio q (in log scale). Note the two properties discussed in the main text: (i) $f_p \to 1$ for $F \to 0$, and (ii) symmetry of f_p about $\log q = 0$ for $F > 1$.
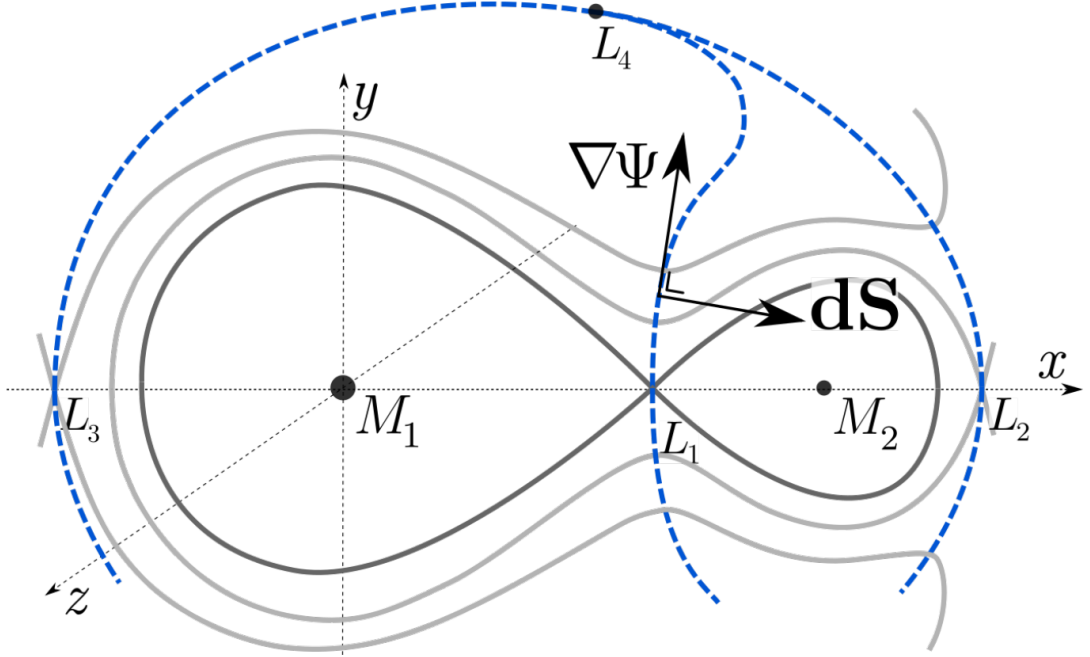
Figure 2.6: Illustration of the difference in modeling geometry of the splitting surfaces in our approach and that of Fabry et al. [2022]. Instead of splitting the two binary components with a plane vertical to the x-axis at the first Lagrange point L_1, the stars in that paper are split by a custom surface $\mathcal{B}$ (dashed blue line) perpendicular to the equipotentials and crossing the x axis at L_1 (see Fig. (2.21). Adapted from Fabry et al. [2022].

stars. In contrast, our work explores the range of models throughout the space of a separation distance between the binary components and examines different contact discontinuity modifications.

In all models of Fabry et al. [2022], the system is considered and mathematically described as a binary system, whereas in our model the system is conceptually and computationally thought of as a significantly deformed star with a hole (see Sec. 2.2 and Fig. 2.2 in particular). Both these approaches have their advantages: Fabry et al.'s treatment will easily enable adding mass transfer prescriptions to the model (this is explicitly planned in further papers in their series); this would be difficult in the model constructed in this thesis and it is beyond its scope. On the other hand, the approach here is more suitable for systems in which one star overflows its Roche lobe and encompasses the other.

Another important distinction is the mass range of focus. Fabry et al. focus on massive stars from 15 $M_\odot$, while in our work we consider stars from 0.3 $M_\odot$ up to 5 $M_\odot$. The choice made by Fabry et al. is motivated by the theoretical assumption that a large fraction of massive binary systems undergoes common envelope evolution. On the other hand, observationally, we only know twelve contact binary systems in that mass range or higher. W UMa stars with low mass in the range studied in this thesis are much more common.

An elegant element in the Fabry et al. [2022] analysis of the contact binary systems has to do with their definition of the boundary $\mathcal{B}$ between the two components. Given the Roche potential Ψ, they choose to define $\mathcal{B}$ using a local

constraint

$$\nabla\Psi \cdot \boldsymbol{dS} = 0, \tag{2.21}$$

where $\boldsymbol{dS}$ is the infinitesimal surface area (in addition, $\mathcal{B}$ is obviously required to pass through L_1). Put in words, the condition (2.21) says that normal to $\mathcal{B}$ is everywhere tangent to the equipotentials of Ψ. The geometry is illustrated in Fig. 2.6. Recall that traditionally $\mathcal{B}$ is simply a plane normal to the axis x dissecting the star at the L_1 point [e.g., Mochnacki, 1984, Marchant et al., 2021]. Firstly, without this choice, the integrated version of Eq. (2.4) would require additional boundary terms allowing to match the structure of the two components at their boundary. With $\mathcal{B}$ defined by (2.21) things are simpler and more elegant. Secondly, the boundary definition in Eq. (2.21) is more natural when one intends to model the mass and energy transfer between the two components. This is because the boundary is set up to be perpendicular to equipotentials allowing simple boundary terms. For instance, in the case of luminosity flow $L_{\mathcal{B}'}$ over the boundary is simply given by

$$L_{\mathcal{B}'} = \int_{\mathcal{B}'} \mathcal{F} \cdot \boldsymbol{dS}, \tag{2.22}$$

where $\mathcal{B}'$ is the small patch of $\mathcal{B}$ around L_1 that truly delimits the component contact area and $\mathcal{F}$ is the radiative flux. As announced in Fabry et al. [2022], these authors intend to develop the analysis in their first paper towards such modelling of transfer processes in massive overcontact binaries. Furthermore, note that the boundary definition using the local condition (2.21) may be also used to connect $\mathcal{B}$ to the outer Lagrange point L_2 (see also Fig. 2.6). This setup of splitting surfaces allows to model stars which overflow not only their Roche lobe, but also the common envelope. However, such a case is less astrophysically motivated, since many different mass loss effects start appearing even before the overflow of the common envelope, and are much more pronounced after this event.

Because of the difference in splitting surfaces, the correction factor solutions coincide only for equipotentials with $F \leq 1$, inside the Roche lobe. Restricting to this interval, a vast majority of the values of f_p and f_T computed by Fabry et al. [2022] are in agreement with the results obtained in this thesis up to errors of order 10^{-5}, in extreme edge cases of mass ratios the agreement is of the order of 10^{-3}.

3. Numerical framework of the stellar models

In this Chapter, we use the formalism developed in Chapter 2 to construct stellar models of a primary component in close binaries (including the common envelope configurations) using the state-of-the-art code MESA (Paxton et al. [2010]) by relaxation from initially isolated, spherical stellar models. Here we primarily describe the way how we construct the models and perform a few tests that help us justify the correctness of the results. Their more complete analysis within the parametric space (q, F) of the Roche model and mass M_1 of the primary is postponed to the next Chapter 4, where we also discuss several recent observational data for which our results may be relevant.

3.1 MESA code specifics

The Kippenhahn averaging formalism, in the form introduced by Endal and Sofia [1976], has been fairly recently implemented in the widely-used and well-tested MESA package, a broad-scope tool for studies in stellar astrophysics [see, e.g., Paxton et al., 2010, 2019]. Their goal was to describe the effects of stellar rotation on its structure. In this default use case, correction factors are calculated from formulas derived from interpolations of Maclaurin spheroids. In this thesis, we aim at a different situation, namely modelling the tidally deformed stellar object in a common envelope stage. To that end, the correction factors f_p and f_T, obtained using integrals evaluated by methods described in the previous Chapter 2, were implemented into the MESA code in a form of large readout tables. Their specific values at an arbitrary cell inside the zone of interest are then obtained by bicubic interpolation using the pre-computed values. This proved to be a much faster method as opposed to our initial idea of calculating everything online in MESA.

MESA stellar code version r15140 has been used for all modelling efforts throughout this thesis.

3.2 Initial conditions

In order to objectively explore stellar models in a certain range of masses, well-chosen initial models had to be used. To get a consistent sample of the main sequence models with different masses, a natural criterion is the hydrogen fraction X reaching a certain reference value. We chose $X = 0.35$ as a suitable threshold of an intermediate-age main sequence star. We used MESA to let isolated, spherical stars of different mass to be evolved from pre-main sequence stages all the way to this intermediate main sequence phase. All models had an initial metallicity value of $Z = 0.02$.

It is both interesting and important to note that the effective temperature of these initial models is not exactly linear function of the mass (see Fig. 3.1). There appears to be a "bump" around 1.2 $M_\odot$ due to the change of dominant nuclear reactions in these stellar models (pp-chain transitioning to the CNO cycle), which
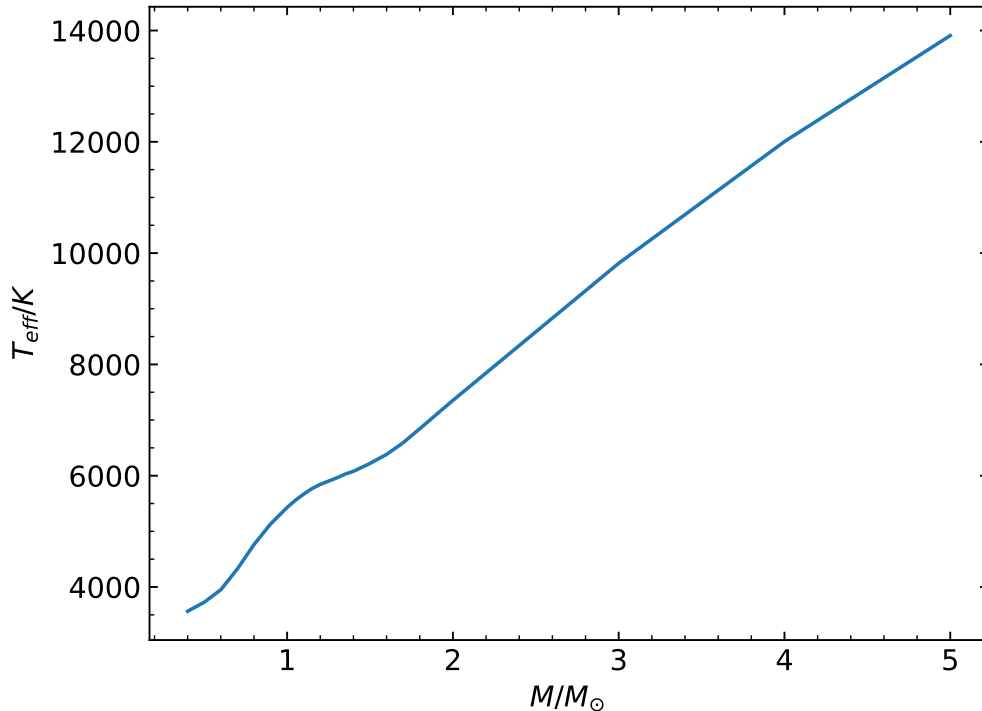
Figure 3.1: Effective temperature of a sample of spherical, isolated stars evolved by MESA to the intermediate age main sequence state (operationally defined by $X = 0.35$; $Z = 0.02$ in all models). Stellar mass at the abscissa. The change in the structure of the models, as to the nature and location of radiative vs convective layers, is reflected in the "bump" of $T(M)$ relation at $M \simeq 1.2$ M$_\odot$.

severely modifies their convective and radiative structure. Since the goal of our work is to construct models of tidally distorted configurations of binaries with common envelopes and analyze their effective surface temperature, the memory of the initial configuration temperature has to be considered if we want to describe the effect of geometry.

3.2.1   Relaxation

In order to understand our procedure, we briefly recall the concept of various relaxation timescales of stellar models and provide their crude estimates. First, the thermal timescale is defined as the timescale over which the energy of the star would be radiated away if nuclear reactions were turned off. For a star of mass M, radius R, and luminosity L, this gives

$$\tau_{\rm th} = \frac{\text{total potential energy}}{\text{rate of energy loss}} \approx \frac{GM^2}{RL}. \tag{3.1}$$

Plugging in the solar values, we get $\tau_{\rm th} \simeq 30$ Myr. Assuming also the characteristic mass-radius and mass-luminosity relations for solar-type stars, namely $R \propto M^{0.8}$ and $L \propto M^4$, we obtain $\tau_{\rm th} \propto M^{-2.8}$, implying that more massive stars a have shorter thermal relaxation timescale (principally because of their huge luminosity).

Second, the dynamical timescale is defined simply as the characteristic length over characteristic velocity, namely the radius over the escape velocity

$$\tau_{\mathrm{dyn}} = \sqrt{\frac{R^3}{2GM}} = \frac{1}{\sqrt{G\bar{\rho}}}, \tag{3.2}$$

where $\bar{\rho}$ is the bulk density. Again, using the solar parameters we get about half an hour. Per its definition, τ_{dyn} coincides with the free fall time. In fact, it is a rough estimate of the longest period helioseismic oscillations, the so-called p-modes. Finally, the nuclear timescale is the longest timescale, which tells us an estimate of a timescale to burn hydrogen content in the star (assuming the main sequence stage). Denoting the energy production rate of the nuclear reactions Q, hydrogen fraction X, and F the fraction of the stellar mass where reactions take place ($F \sim 0.1$, say), we have

$$\tau_{\mathrm{nuc}} = \frac{MXF}{\frac{L}{Q}}. \tag{3.3}$$

The Sun has $\tau_{\mathrm{nuc}} \simeq 10$ Gyr, a rough estimate of the time it spends on the main sequence. Therefore, we verified the strong ordering $\tau_{\mathrm{dyn}} \ll \tau_{\mathrm{th}} \ll \tau_{\mathrm{nuc}}$.

Let us return now to our goal, namely to construct a quasi-stationary model of a tidally deformed primary in a close binary. We borrow the sample of spherically symmetric models described in Sec. 3.2 and use them as the initial stellar-structure model. Then we define a certain binary configuration, basically by the mass ratio q and the fill-out factor F, and use the Roche potential to define the spatial geometry of the layers in the final model. The initial state is then let by MESA to relax over a certain time into the desired distorted configuration. The question is what timescale is the most relevant for this task? Since we aim at a stationary model with a correct structure of thermodynamical parameters, the thermal relaxation timescale appears to be the right guess. Changes in chemical composition, occurring on a nuclear production timescale, result in a long-term evolution of the stellar parameters. As we have seen above, the characteristic timescale of this slow evolution is much longer than the thermal timescale. So even if the composition changes cannot be frozen in a consistent model, one can adopt an approximation of a slow, adiabatic evolution through a sequence of thermally relaxed states with fixed chemistry. In order to ensure stability, time-step controls were set up so that at least 20 steps are made throughout the relaxation procedure. Trials and tests have shown that this choice was satisfactory, and further smoothing in time did not provide changes in results.

Figure 3.2 shows a satisfactory relaxation of the effective temperature for primaries of two different masses: 1 $M_{\odot}$ and 5 $M_{\odot}$. In both cases, we assume a secondary with $q = 0.5$, and their distance implies a binary configuration having a fill-out factor $F = 0.9$. The thermal timescale is highlighted in red. By this time, the temperature (and similarly all other important parameters) have relaxed to a steady value. The relaxation procedure is run through three thermal timescales to ensure higher precision. The evolution of the radius through the relaxation procedure serves as a consistency check. This is because the volume should not change much, only the geometry it occupies changes. In most cases, the radius stayed within 1% of its initial value.

Another indicator confirming that the thermal timescale is sufficient for the relaxation processes has to do with the outer convective layer (we argue below that this zone plays an important role in the analysis of contact binaries and systems with a common envelope). The extent of this layer converged around the thermal timescale in all models. Figure 3.3 demonstrates the process of the surface convective layer relaxation for a solar mass star in the same configuration as in Fig. 3.2.

Evolution with chemical changes was also briefly tested. Alongside with thermal relaxation described above, a long-term effect was observed, which caused the observed stellar parameters, such as temperature, to not asymptotically converge but undergo a very slow, secular evolution.
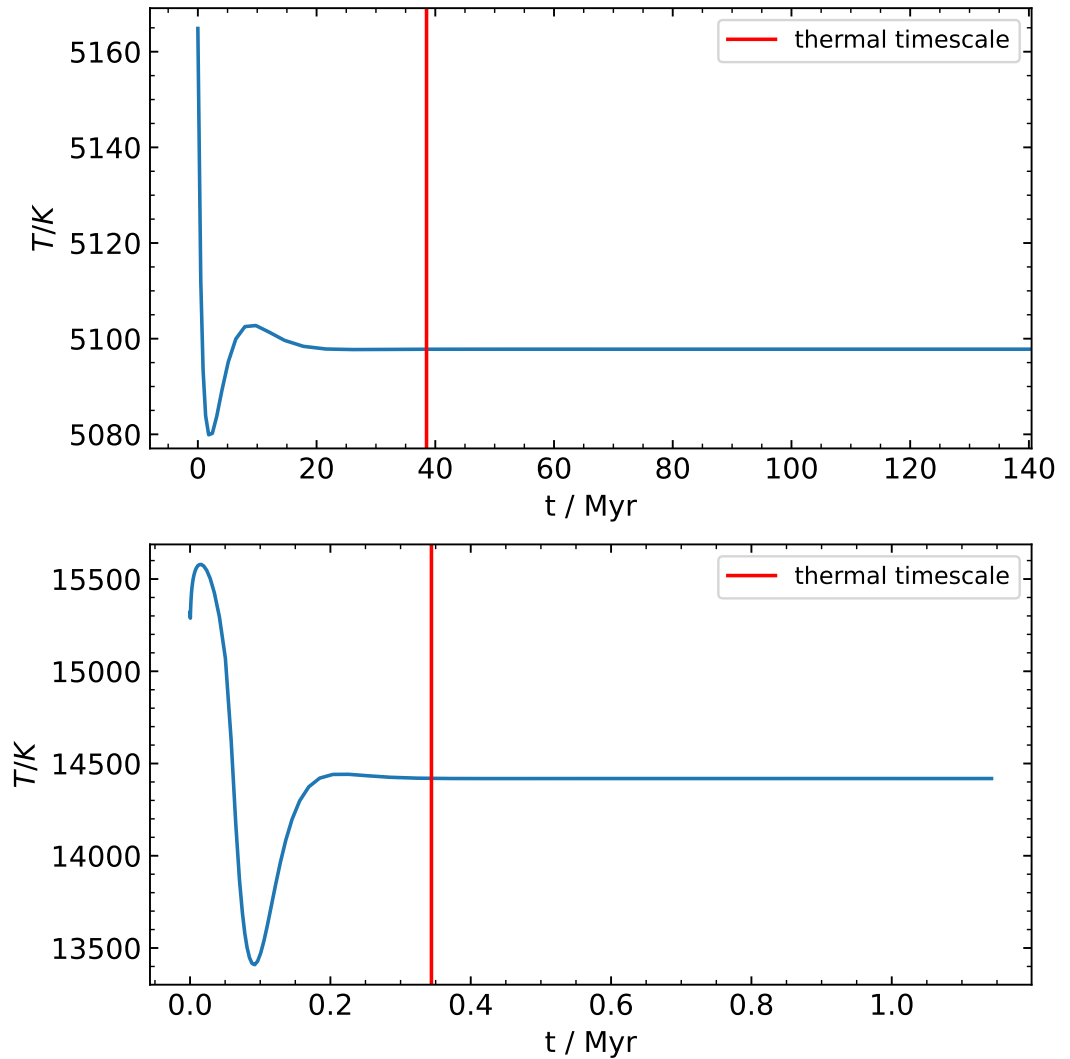
Figure 3.2: Example of the relaxation phase for stars of mass 1 $M_\odot$ (top) and 5 $M_\odot$ (bottom). The abscissa is time t in Myr, the ordinate shows the effective temperature in K. In both cases, a secondary with $q = 0.5$ generates the tidal deformation, and the binary configuration has a fill-out factor $F = 0.9$. The relaxation was satisfactorily completed by reaching the thermal timescale, shown here by the red line. Other important stellar parameters follow similar evolutionary tracks.

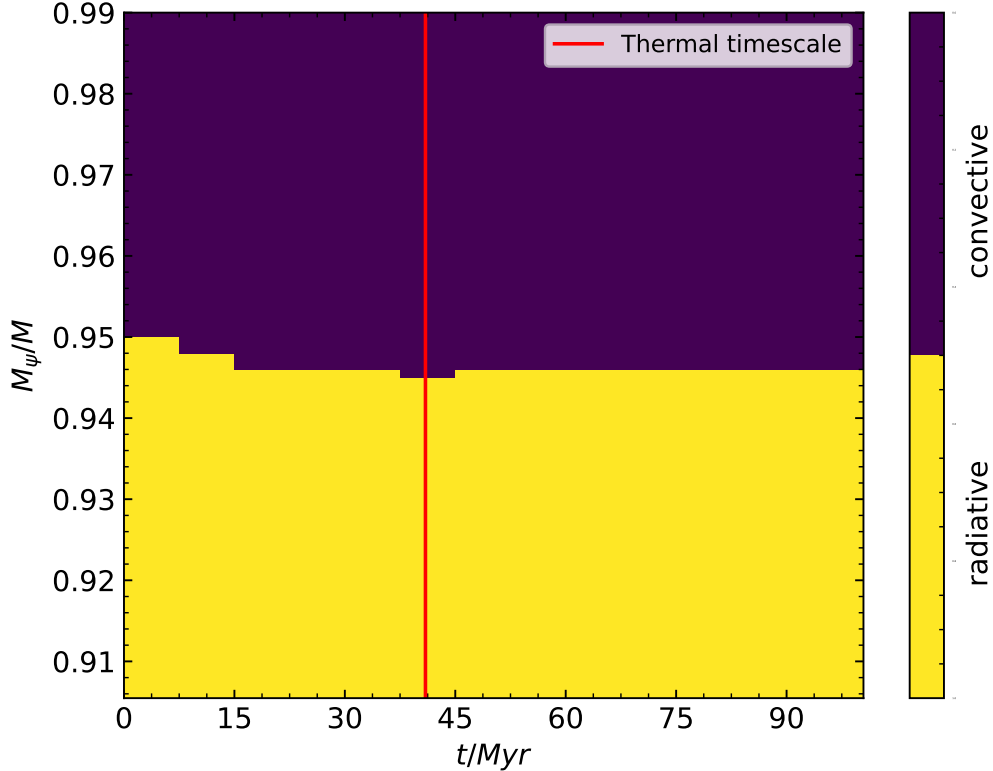Figure 3.3: Example of a relaxation procedure of the surface convective layer (violet) over a radiative deeper zone (yellow) for a star of mass 1 $M_\odot$ within a close binary system with $q = 0.5$ and the fill-out factor $F = 0.9$ (as in Fig. 3.2). The abscissa is time in Myr and the ordinate shows the mass M_Ψ within the near-surface equipotentials expressed in the total stellar mass. The thermal timescale (shown by the red line) is clearly sufficient to relax the model to a quasi-stationary state.

3.3 Important features of MESA

Our contribution to the structure of the models constructed in this thesis consists primarily in the determination of the correction factors f_p and f_T for a wide range of q and F values, and their implementation into the MESA code. However, other aspects of the stellar model remain as they were implemented into MESA by many previous contributors. Here we recall only the most important for our analysis.

Equations of state used by MESA are a mix of many formulations, depending on thermodynamical parameters, as well as hydrogen fraction and metalicity. The main ingredients are OPAL (Rogers and Nayfonov [2002]), PC (Potekhin and Chabrier [2010]), FreeEOS, Skye (Jermyn et al. [2021]), and HELM (Timmes and Swesty [2000]). The specific usage of various equations of state in MESA is thoroughly described in Paxton et al. [2019].

The default MESA opacity is a mixture of many prescriptions. The total opacity is a combination of radiative and conductive opacities

$$\frac{1}{\kappa} = \frac{1}{\kappa_{\rm rad}} + \frac{1}{\kappa_{\rm cond}}, \tag{3.4}$$

31

where the radiative opacity is the Rosseland mean opacity is taken from tables based on metalicity and hydrogen fraction from Iglesias and Rogers [1996] and Ferguson et al. [2005]. The conductive opacity is given by the conductivity K as

$$\kappa_{\mathrm{cond}} = \frac{16\sigma_{\mathrm{SB}}T^3}{\rho K}. \tag{3.5}$$

which is interpolated from a table calculated by Cassisi et al. [2007] (σ_{SB} is the Stefan–Boltzmann constant).

The choice of the nuclear reaction chain is not relevant since chemical changes are suppressed during relaxation, which occurs only on the thermal timescale.

All models examined in this thesis have an initial metalicity of $Z = 0.02$. No winds or mass loss prescriptions are used in these models.

Atmosphere is chosen as the Eddington atmosphere [see, e.g., Cox and Giuli, 1968]. Standard boundary conditions in MESA are those interpolated on a grid of pressure and temperature. A more thorough explanation is given in the next Section. A sample MESA inlist is included in Appendix B.

3.3.1 Exterior boundary conditions from Fabry et al.(2022)

While the central boundary conditions are obvious, the choice of the exterior boundary conditions has to be done with caution when dealing with tidal deformation. A recipe for generally non-spherical stars was developed by Fabry et al. [2022], and here we shall adapt it to the tidally deformed configuration relevant to this thesis. In spite of its simplicity, the gray plane parallel Eddington atmosphere Rybicki and Lightman [2004] is a standard assumption in stellar-structure models. In this approximation, the atmosphere is assumed to be in thermal radiative equilibrium, and the absorption coefficient α is constant (and there is no frequency dependence in any of the variables). This set of conditions implies that the source function is simply Planck's black-body law.

Traditionally, stellar codes consider the optical thickness from $\tau = 0$ far away to some nominal value (usually around 1), where the stellar boundary is defined. If the geometry is not spherical, different regions get to this critical optical depth at different equipotentials - the equipotentials do not coincide with surfaces of constant optical depth. To express this mathematically, in the tidally deformed case, the differential of the optical depth is modified by the geometry as ($\alpha = \kappa\rho$, where κ is the opacity)

$$d\tau = \kappa\rho\,dz = -\kappa\rho\frac{dn}{d\Psi}\,d\Psi = -\kappa\rho g^{-1}d\Psi. \tag{3.6}$$

Following the recipe in Fabry et al. [2022], we first define the global effective temperature $T_{\mathrm{eff},\Psi}$ of an equipotential by comparing the total, bolometric radiative flux to that of black body using the Stefan-Boltzmann law. We obtain

$$L_\Psi = \int_\Psi \mathcal{F}d\sigma \equiv S_\Psi\,\sigma_{\mathrm{SB}}T^4_{\mathrm{eff},\Psi}. \tag{3.7}$$

Note the equipotential does not have to be spherical and its total surface area S_Ψ is generally given by Eq. (2.18) ($\mathcal{F}$ is the scalar radiation flux through normal to the surface area). At the same time, the local effective temperature variations on

the chosen equipotential can also be defined with Eq. (3.6). Since the radiative flux $\mathcal{F}$ is proportional to the gradient of the potential, the local effective surface temperature $T_{\text{eff},l}$ can be defined as follows

$$\mathcal{F} = \frac{g}{\langle g \rangle} \sigma_{\text{SB}} T_{\text{eff},\Psi}^4 = \sigma_{\text{SB}} T_{\text{eff},l}^4. \tag{3.8}$$

Assuming the expression for radiation pressure

$$P_r(\tau) = \frac{4\sigma_{\text{SB}}}{3c} T^4(\tau). \tag{3.9}$$

where c is the speed of light, and considering the pressure at the $\tau = 0$ surface from Cox and Giuli [1968] (which is a simple consequence of the assumption of isotropic radiation outwards, therefore no limb darkening effects, often stated as Lambert's law), we also have

$$P_r(0) = \frac{2\mathcal{F}}{3c}. \tag{3.10}$$

The temperature profile of a grey atmosphere can be written as

$$T^4(\tau) = \frac{1}{2} T_{\text{eff},l}^4 \left(1 + \frac{3}{2}\tau\right). \tag{3.11}$$

where it is assumed that $\tau_{\text{surf}} = 2/3$. Putting $T_{\text{surf}} = T_{\text{eff},\Psi}$ gives the first boundary condition for the surface temperature.

In order to obtain the other boundary condition for pressure, we can use the equation of hydrostatic equilibrium:

$$\frac{dP}{d\tau} = \frac{g}{\kappa}. \tag{3.12}$$

The pressure can then be integrated from $\tau = 0$ to the boundary value of $\tau = 2/3$. Because of the validity of the boundary condition for temperature, the gravity at the surface can be taken as $\langle g \rangle$, if integrating to a point where $T_{\text{eff},\Psi} = T_{\text{eff},l}$, which necessarily exists. The calculation is significantly simplified if one assumes a constant opacity and gravity in a thin atmosphere:

$$P_p = \int_0^{\tau_{\text{surf}}} \frac{\langle g \rangle}{\kappa} d\tau + P_r(0) = \frac{2}{3} \frac{4\pi G M_\Psi}{\kappa S_\Psi} \frac{f_p}{f_T} + \frac{2}{3} \frac{\sigma_{\text{SB}} T_{\text{surf}}^4}{c} \tag{3.13}$$

This approach leads to a complete set of outer boundary conditions for the pressure and temperature

$$P_{\text{surf}} = \frac{2}{3} \frac{4\pi G M_\Psi}{\kappa\left(T_{\text{surf}}, P_{\text{surf}}\right) S_\Psi} \frac{f_p}{f_T} + \frac{2}{3} \frac{\sigma_{\text{SB}} T_{\text{surf}}^4}{c},$$

$$T_{\text{surf}} = \sqrt[4]{\frac{L_\Psi}{\sigma S_\Psi}}. \tag{3.14}$$

4. Results

In this chapter, we analyze the results of the stellar models for the primary component in short-period binaries computed using our simple 1D approach implemented into the MESA code. We explore their dependence on three parameters. The first two determine the Roche model geometry: (i) mass ratio q of the two components in the binary, and (ii) the equipotential value C of the surface of the modeled star. The latter –(ii)– may also be expressed using the fill-out factor $F(C)$, and given its value we may have configurations ranging from a detached situation of a primary deformed by the secondary up to a common envelope geometry. Alternatively, we also use the distance of the components normalized to the radius of the spherical counterpart d/R_∞ in the binary as a measure of C or $F(C)$, since there is a one-to-one correspondence of all these parameters. The third parameter is the mass M_1 of the primary. This choice may appear redundant because M_1 scaled out from the Roche model itself (being represented just by the mass ratio q). However, other important details of the stellar structure, such as the existence and location of the convective zones, do additionally depend on M_1 uniquely. Therefore, we need to add M_1 as an independent parameter.

In the next few Sections 4.1 to 4.5, we first fix $q = 0.5$ and consider different geometric configurations by changing the fill-out factor F or d. We also consider the dependence of the results on the exterior boundary conditions for the stellar model and different M_1 values. Next, we explore results for other q values, roughly bracketing the range of the observed systems (i.e., from 0.1 to 1).

Finally in Section 4.6, we try to connect our results with observations pouring out from sky surveys in the past decade. Due to the simplicity of our model, this part should be considered as a hint for avenues to be studied in the future by more complete approaches rather than a definitive solution.

4.1 Detached configuration

A sample model of a 1 $M_\odot$ star with a 0.5 $M_\odot$ companion in the detached configuration with a separation of $d = 2.5$ $R_\odot$ (corresponding to a fill-out factor F of roughly 0.9 and a binary period of $\simeq 0.25$ d) is shown in Fig. 4.1, where it is compared with a non-deformed spherical star of the same mass. The first two panels show the profile of the temperature and density in the upper layers of the star. Luminosity is shown throughout the whole star as the variability is negligible in the final interval. The last two panels show the behavior of the correction factors f_p and f_T. The spherical model has them equal to unity throughout the whole volume by definition, but the tidally deformed model has $f_p \simeq f_T \simeq 1$ only at the very center of the star. Both values become gradually smaller than unity as the equipotentials start to deviate from spheres near the surface.

Overall, the tidal deformation effects on the internal structure of the primary are not too significant in this case. This is because the system is well detached and the deformation is not too large. Note the minimum value of f_p is only $\simeq 0.94$ (Fig. 4.1).
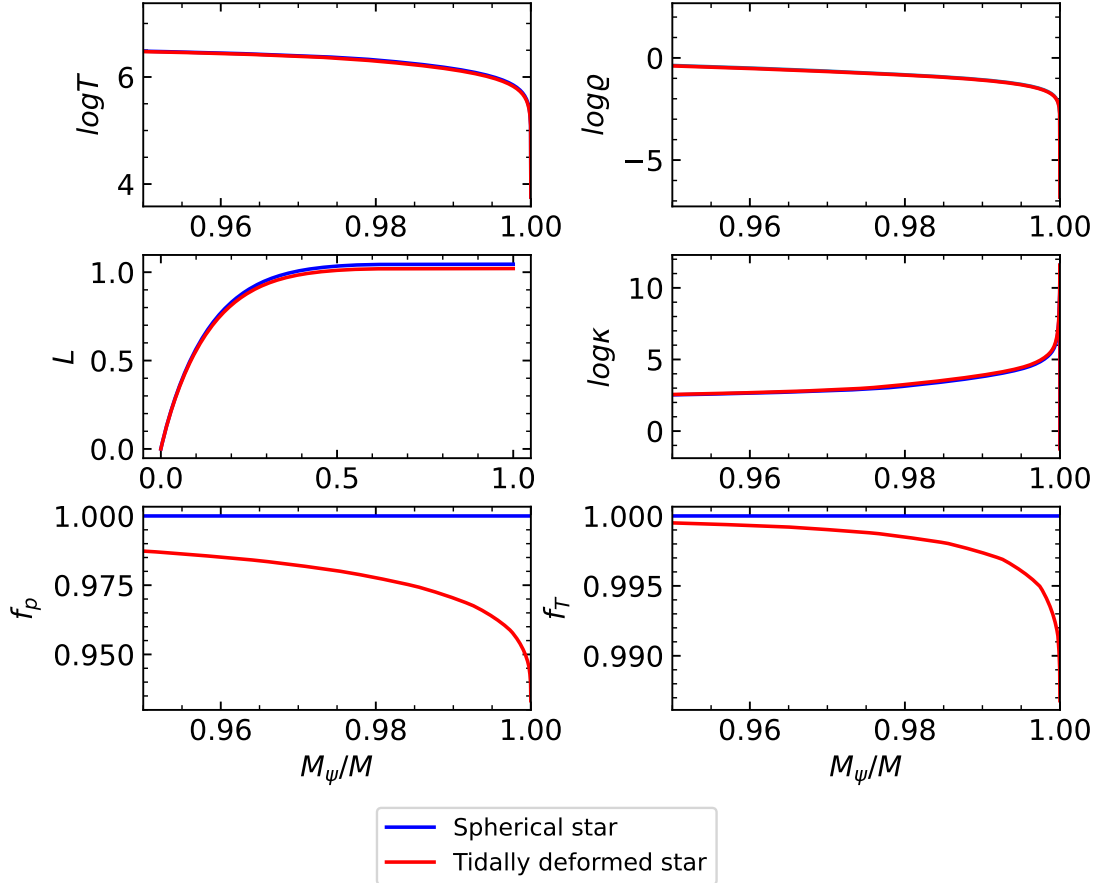
Figure 4.1: Internal structure of a spherical (blue) and tidally deformed (red) star in a detached configuration with $M_1 = 1$ $M_\odot$, $q = 0.5$ and $F \simeq 0.9$. From top left to bottom right, the panels show: the temperature (in K), the density (in g/cm^3), the luminosity (in $L_\odot$), the opacity (in cm^2/g), and the correction factors f_p and f_T in the last row. All variables are shown as a function of the mass M_Ψ inside a given Roche equipotential normalized by the total mass of the star $M = 1$ $M_\odot$.

4.2 Contact configuration

Next, we consider a more extreme case of a contact binary in a common envelope configuration. We keep the masses 1 $M_\odot$ with a 0.5 $M_\odot$ for the primary and the secondary components, thence $q = 0.5$, but set their separation to $d = 1.7$ $R_\odot$ only. These parameters define a contact configuration with $F \simeq 1.4$ and a binary period of $\simeq 0.14$ d. Figure 4.2 shows behaviour of selected variables inside the primary, which can be directly compared to Fig. 4.1. There is only a certain difference to be noted on the scale shown (though more than in Fig. 4.1), apart from a behavior of the correction factors f_p and f_T which now drop to significant minima $f_p \simeq 0.84$ and $f_T \simeq 0.62$ at the inner critical equipotential of the Roche model. Note that the total mass of the common envelope in our model is tiny, only $\simeq 0.001 - 0.002$ $M_\odot$. Given the typically huge mass concentration towards the center of stars, this is not that surprising.
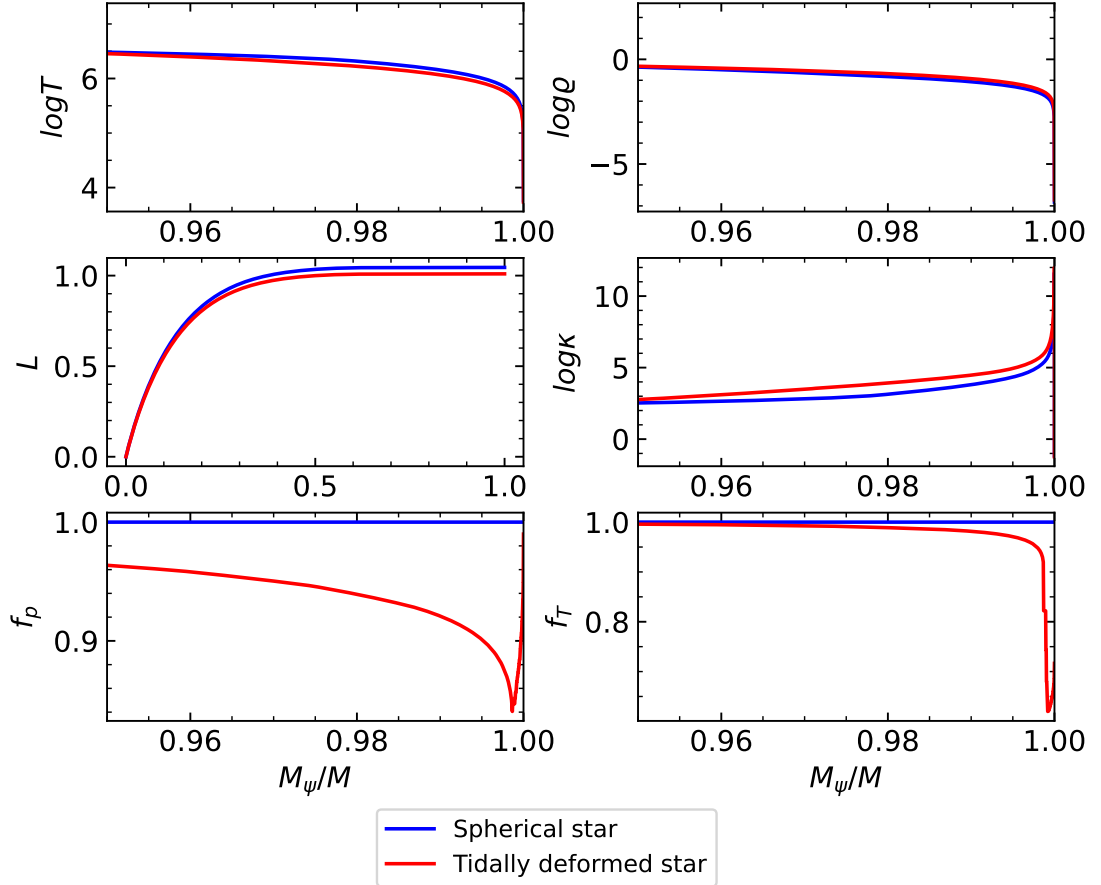
Figure 4.2: Internal structure of a spherical (blue) and tidally deformed (red) star in a contact configuration with $M_1 = 1$ $M_\odot$, $q = 0.5$ and $F \simeq 1.4$. From top left to bottom right, the panels show: the temperature (in K), the density (in g/cm^3), the luminosity (in $L_\odot$), the opacity (in cm^2/g), and the correction factors f_p and f_T in the last row. All variables are shown as a function of the mass M_Ψ inside a given Roche equipotential normalized by the total mass of the star $M = 1$ $M_\odot$. The inner critical equipotential of the Roche model is located at the minima of f_p and f_T.

4.2.1 Conditions at Roche lobe overflow

In contact configurations, some equipotential parameters change discontinuously, or at least discontinuously in the first derivative at the Roche lobe equipotential. Naturally, when adding the second star, the surface area, the average gravity, and average inverse gravity all experience a discontinuity at this point. Recalling our approximation discussed in Sec. 2.2, we subtract the volume of the secondary Roche lobe from the overfilling equipotentials, making thus the effective radius r_Ψ continuous, and we also do not increment M_Ψ by the secondary mass at that point. In the same way, the luminosity from the secondary is added to the primary budget of L_Ψ. Nevertheless, the role of these apparent discontinuities in some of the model parameters warrants a comment, as they may potentially trouble the solution of the internal structure.

Denote the surface area, average gravity, and average inverse gravity as in Chapter 2. Then using index 1 for the primary Roche lobe, index 2 for the secondary Roche lobe, and primed variables for parameters corresponding to the first equipotential of the common envelope just above the Roche lobes, we can approximate the boundary conditions at Roche lobe overflow as follows

$$S' \left\langle g^{-1\prime} \right\rangle \simeq S_1 \left\langle g^{-1} \right\rangle_1 + S_2 \left\langle g^{-1} \right\rangle_2 , \tag{4.1}$$

and analogously for the gravity $\langle g \rangle$. In our model, the radius does not change. Inserting this estimate into equations (2.6) and (2.10) for the correction factors, one obtains

$$f_p' = \frac{4\pi r_\psi^4}{GM_\psi S_\psi} \frac{1}{\langle g^{-1} \rangle} \simeq f_p \left[(1 + M_2/M_1)(1 + S_2/S_1) \right]^{-1} < f_p, \tag{4.2}$$

$$f_T' = \left(\frac{4\pi r_\psi^2}{S_\psi} \right)^2 \frac{1}{\langle g \rangle \langle g^{-1} \rangle} \simeq f_T \left[1 + \frac{S_2 \langle g \rangle_2}{S_1 \langle g \rangle_1} \right]^{-1} \left[1 + \frac{S_2 \langle g^{-1} \rangle_2}{S_1 \langle g^{-1} \rangle_1} \right]^{-1} < f_T, \tag{4.3}$$

where f_p and f_T on the right hand sides of these equations are the values for the inner critical equipotential of the Roche model. We can clearly see that both correction factors will drop above the inner critical equipotential, and the significance of the jump depends on the mass ratio and mainly the ratio of Roche lobe surfaces. Usually, the jump will be more significant in f_T than f_p (see Fig. 2.3). The magnitude of most of the computed jumps are in accordance with estimates in Eqs. 4.2 and 4.3 within 10-20%.

However, in the case of our model, which does not use a single Roche potential (see the last paragraph in Sec. 2.2), the discontinuities apparently smoothen out when compared to the equations above. Due to the relaxation procedure, all the thermodynamical quantities do not experience any discontinuities or even discontinuities in their derivative. The jump in f_p than f_T also gets smoothened out, leaving just a discontinuity in the derivative. This is in contrast with conclusions in several references mentioned in Chapter 1, where the effects such as density inversion zones in the common envelope were predicted. Regardless, it is interesting to see that hydrodynamically and thermally stable common envelope models are possible without derivative discontinuities.

4.2.2   Relevance of boundary conditions

To examine the effect of the exterior boundary conditions, models with standard boundary conditions were compared with those derived in Section 3.3.1. To keep things simple, in particular, to distill the proper effects of boundary conditions, we used the same contact configuration as in Section 4.2, namely $M_1 = 1\ \mathrm{M_\odot}$, $q = 0.5$, and $F = 1.4$. We only changed the exterior boundary conditions of the model. Therefore, we used our improved set, basically replotting the red profiles from Fig. 4.2, and compared it with the standard, simplified set. Results are shown in Fig. 4.3. The differences are tiny, except for the fact that the model with the standard boundary conditions appears to predict about twice as much mass in the common envelope if compared to the new model.
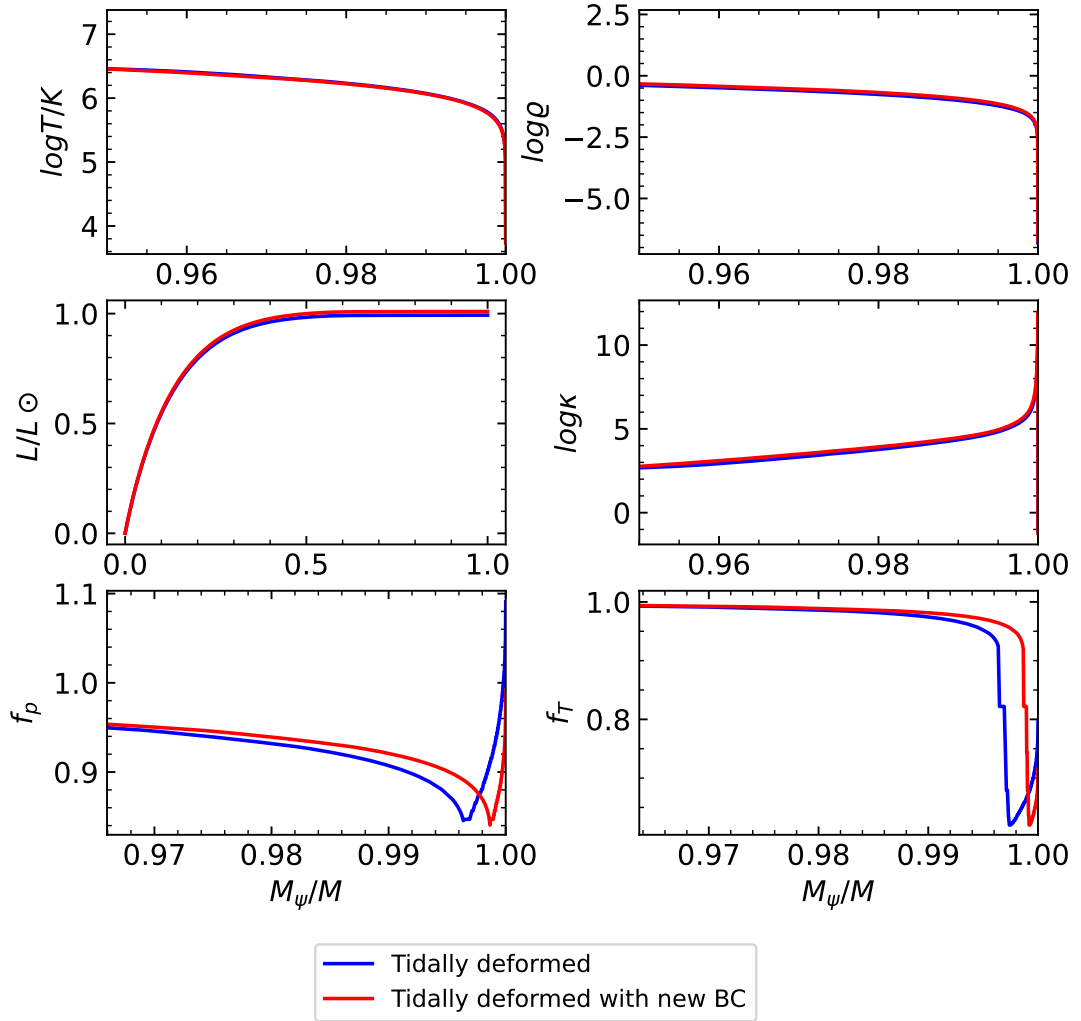
Figure 4.3: The role of the old (blue) and new (red) formulation of the exterior boundary conditions on the internal structure of a star in a contact configuration with $M_1 = 1$ M$_\odot$, $q = 0.5$ and $F \simeq 1.4$. From top left to bottom right, the panels show: the temperature (in K), the density (in g/cm^3), the luminosity (in $L_\odot$), the opacity (in cm^2/g), and the correction factors f_p and f_T in the last row. All variables are shown as a function of the mass M_Ψ inside a given Roche equipotential normalized by the total mass of the star $M = 1$ M$_\odot$. The inner critical equipotential of the Roche model is located at the minima of f_p and f_T.

4.3 Geometric effects in convective structure

Tidal deformation can significantly modify and adjust the thickness and configuration of convective and radiative zones in stars. In MESA, the Ledoux criterion (Ledoux [1947]) is generally used to determine whether a particular zone in the star is convective or radiative. To keep things simple, we shall, however, assume local chemical homogeneity. In this situation, the Ledoux criterion takes the classical (and simpler) Schwarzschild form.

Within the Kippenhahn averaging formalism, the traditional radiative gradient

of the energy transport is modified by a multiplicative factor f_T/f_p (Eq. (2.11)). The adiabatic gradient is local and no modifications are needed. Therefore, the onset of convection occurs when

$$\nabla_{\text{ad}} < \nabla_{\text{rad}} \frac{f_T}{f_p}, \qquad (4.4)$$

where ∇_{ad} and ∇_{rad} are the adiabatic and radiative temperature gradients. The former depends principally on the equation of state assumed, and MESA code has its own routines to handle it. The latter is given readily by Eq. (1.1). For sake of completeness, we note that the additional, geometric factor f_T/f_p can be rewritten in terms of equipotential parameters

$$\frac{f_T}{f_p} = \frac{4\pi G M_\psi}{S_\psi g_\psi}. \qquad (4.5)$$

It turns out that the configurations with the fill-out factor $F \geq 1$, namely in the common envelope state, $f_T/f_p < 1$ typically. Finally, we note the important parametric dependence of (i) $\nabla_{\text{rad}} \propto \kappa$ on the opacity κ, and (ii) $\nabla_{\text{ad}} \propto c_P^{-1}$ on the heat capacity c_P. Convection is thus promoted by either large κ or large c_P values. Especially the first case is important for the surface layers of star models we are dealing with.
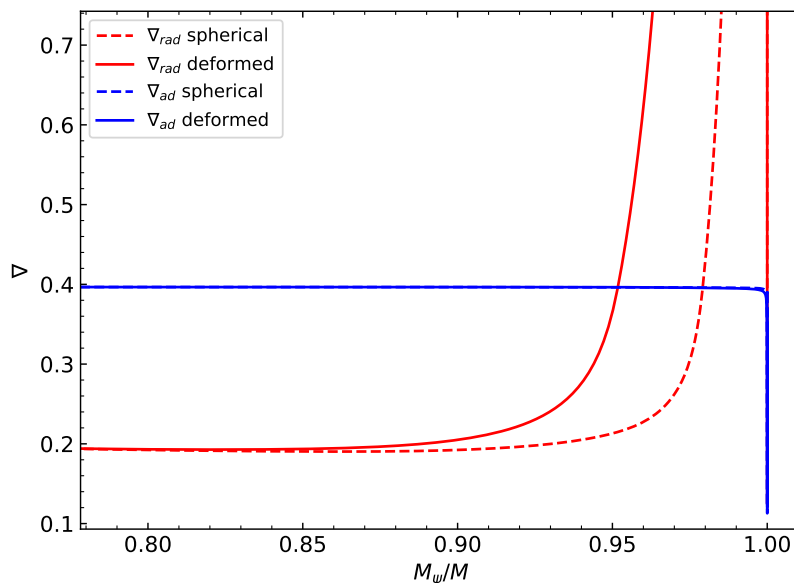
Figure 4.4: Illustration of radiative and adiabatic gradients in spherical and tidally deformed stars (the radiative gradient contains the correction-factor term f_T/f_p in the tidally deformed case). We can clearly see that the biggest change is in the radiative gradient, associated with a significant increase in opacity in the tidally deformed model. The subsurface convection layer is therefore deeper in this case.

A closer look at the adiabatic and radiative gradients is shown in Fig. 4.4. The value of these gradients in the surface layers representing the last 25% of the star in terms of mass is shown for the contact system with the same parameters as in Fig. 4.2 ($M_1 = 1\ \text{M}_\odot$, $q = 0.5$ and $F \simeq 1.4$). Dashed lines show the gradients

for the spherical star, whereas full lines are gradients of the tidally deformed contact configuration. The adiabatic gradients shown in blue coincide very closely throughout the whole star. The radiative gradients, however, differ significantly in the last 20% of the star in terms of mass coordinate. We may note that the subsurface convection onsets earlier in the tidally deformed model than in the spherically symmetric model of an isolated star.

A detail of the behavior of the surface convective layer for a 1 $M_\odot$ star tidally deformed by a 0.5 $M_\odot$ companion is shown in Fig. 4.5. Interestingly, as the secondary gets closer, the thickness of the convective layer increases. The most significant gradient in the depth of the convective zone occurs near the inner critical configuration. For a typical contact state, the mass of the surface convective zone roughly doubles that of the isolated star.
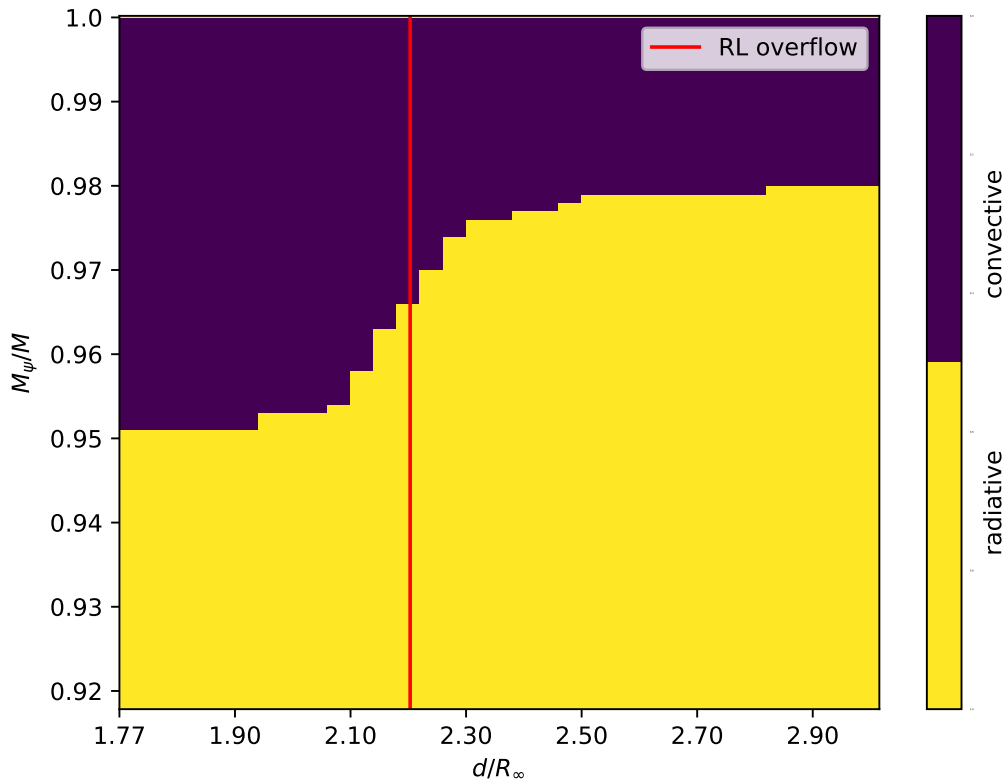

Figure 4.5: Example of the behavior of the surface convective layer (violet) over a radiative deeper zone (yellow) for a star of mass 1 $M_\odot$ tidally deformed by a 0.5 $M_\odot$ companion ($q = 0.5$). The abscissa shows the separation d of the two stars (normalized to the radius R_∞ of a non-deformed, isolated star) and the ordinate shows the mass M_Ψ within the near-surface equipotentials of the primary expressed in the total stellar mass. In our approach, only the structure of the primary is modelled, while the secondary is a point mass. The sequence of models from right to left in the figure corresponds first to a detached state with the primary only deformed by the secondary. After overflowing its Roche lobe (shown by the red vertical line), the system transitions into a common envelope configuration. The leftmost state corresponds to a near common envelope overflow phase - fill-out factor $F \simeq 2$. The subsurface convective zone becomes deeper in the common envelope phase.

4.4 Analysis for $q = 0.5$

An analysis of tidally deformed stellar models was made for twenty-five different masses M_1 ranging from 0.3 to 5 M$_\odot$, with a majority covering the interval of $1 - 1.5$ M$_\odot$ which is the most interesting range. Models of different separations, thus fill-out factors, were examined.
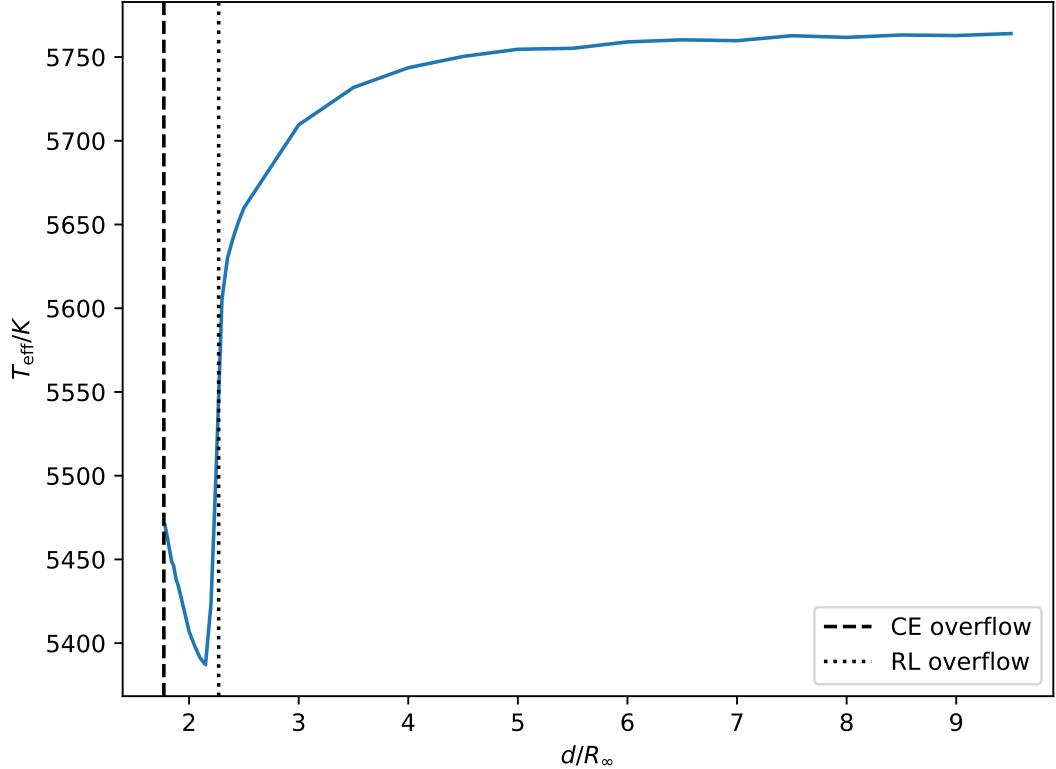

Figure 4.6: The effective temperature as a function of the separation d of the two stars (normalized to the radius R_∞ of a non-deformed, isolated star) is plotted for systems with mass ratio $q = 0.5$ and $M_1 = 1$ M$_\odot$. The onset of the two key configurations - the Roche lobe overflow and the common envelope overflow - are shown with dotted and dashed lines respectively. Note the rapid drop of the effective temperature as soon as the mass starts to overflow the Roche lobe. While the temperature increases along the common envelope configuration sequence with an increasing fill-out factor, it still remains by more than 350 K smaller than the asymptotic value corresponding to the isolated primary.

Before we overview results for the range of stellar mass, we first get an insight from a configuration of $M_1 = 1$ M$_\odot$ primary accompanied with a secondary of 0.5 M$_\odot$ mass (thus $q = 0.5$). We follow a sequence of binaries in which we change the separation d from $d/R_\infty = 10$ to the smallest possible value for which the binary start to overflow the outer critical Roche equipotential at L_2 point. Put in other words, the sequence also corresponds to configurations with the fill-out factor ranging basically from 0 to 2. In Fig. 4.6 we plot the effective temperature T_eff of the primary as a function of d. Obviously, at large separation the tidal effect of the secondary is tiny and the star behaves like an isolated object (see the reference temperature in Fig. 3.1). As the primary becomes deformed at smaller separations,

T_{eff} decreases. This is likely because of the surface area of the deformed primary increases. This effect accelerates at the inner critical equipotential configuration ($F = 1$), for which the drop in T_{eff} with respect to its isolated counterpart is $\simeq 350$ K. This is perhaps again the effect of a rapid expansion of the exterior surface of the contact binary. As the components continue to be closer to each other, the fill-out factor increases to 2, and T_{eff} starts slightly increasing. Not only does the exterior surface slightly compactify, but the effect may also be due to the gradually deeper subsurface convection zone that brings hotter material from deeper layers to the surface.
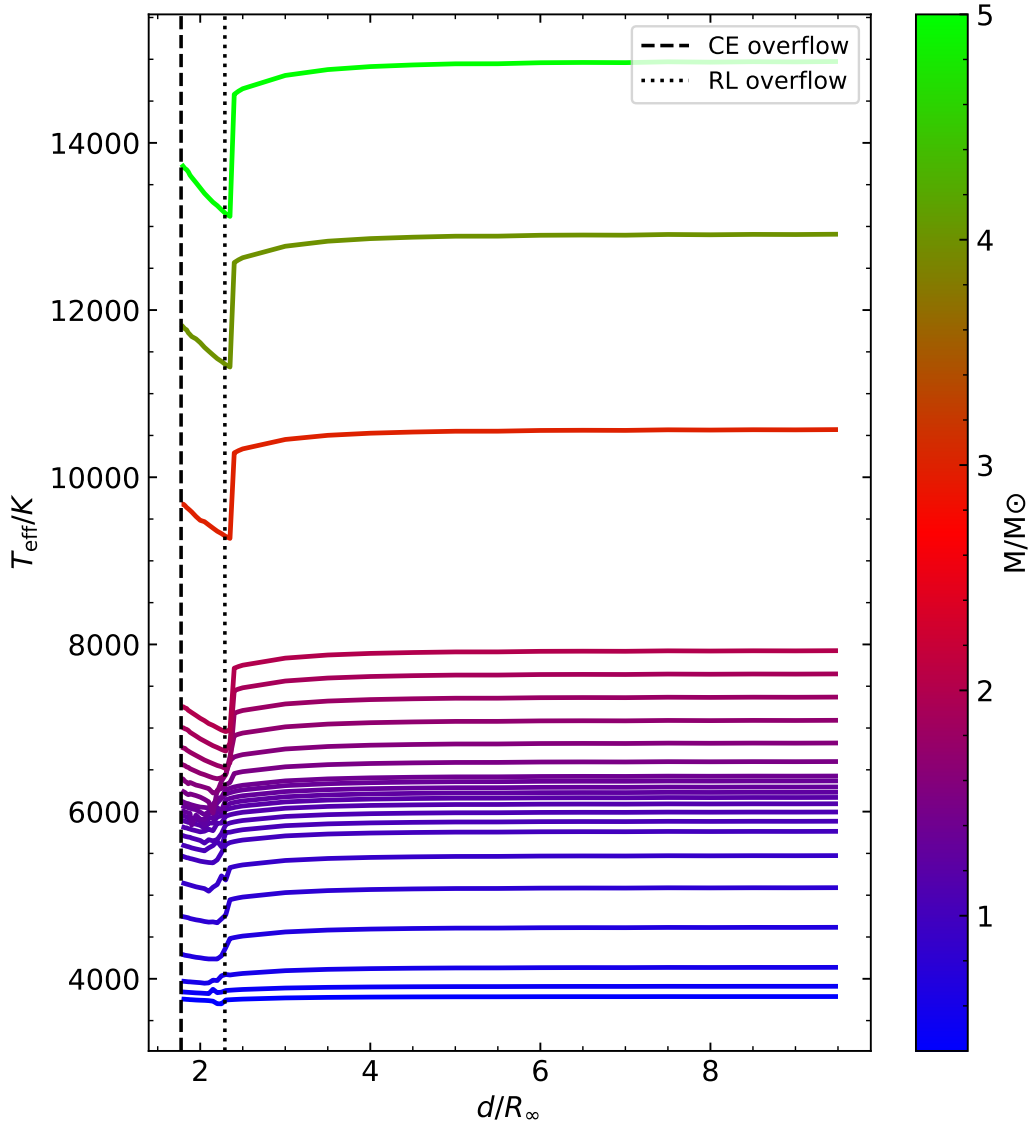
Figure 4.7: The effective temperature as a function of the separation d of the two stars (normalized to the radius R_∞ of a non-deformed, isolated star). This is similar to Fig. 4.6, but now shown for various masses M_1 in between 0.3 M$_\odot$ to 5 M$_\odot$ (all binaries assumed to have $q = 0.5$). The Roche lobe overflow limit is shown with a dotted line, common envelope overflow limit with a dashed line (terminal configuration of our models). The temperature drop at the inner critical limit appears to be much larger for more massive stars.

In Fig. 4.7 the T_{eff} versus d dependence illustrated in Fig. 4.6 is plotted for the whole range of primary masses M_1, namely in between 0.3 $M_\odot$ to 5 $M_\odot$. There are obvious similarities and also interesting differences for different M_1 values. First, T_{eff} always decreases with decreasing d, having a major drop at the binary configuration corresponding to the inner critical case. Below this distance, T_{eff} tends to increase. However, the effect is much smaller for low-mass stars. Additionally, the progression towards the high-mass stars is not a continuous increase of the effect. This is because the effects become anomalously small again when $M_1 \simeq 1.3$ $M_\odot$, before steadily increasing for larger M_1.
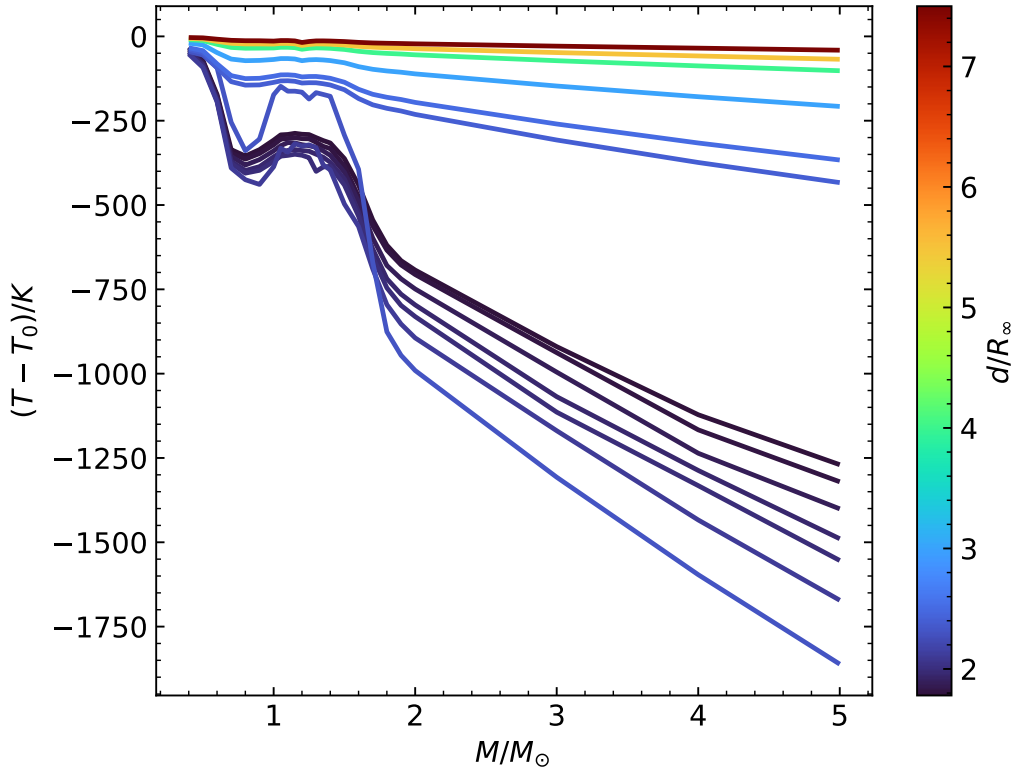

Figure 4.8: The difference between the effective temperature T_{eff} of the relaxed, tidally deformed model and that of the isolated, spherical model from Fig. 3.1 with the same mass (at the abscissa). Different curves for different separations in the binary configuration with $q = 0.5$ (color-coded using the bar at the right). Different separations map uniquely onto configurations with different fill-out factors. At the largest separation (dark red) the difference is essentially zero since the star is very close to its spherical state. Note the significant jump in temperature near the inner critical Roche limit (blue curves and separation $d/R_\infty \simeq 2.25$). This effect appears to be suppressed for stars with M_1 in the 1 $M_\odot$ to 1.6 $M_\odot$ range, in which the quasi-linear dependence $T_{\text{eff}} - T_0 \propto M_1$ at each separation is disrupted by significant a bump.

This behaviour is actually better seen on Fig. 4.8, where we show a difference $T_{\text{eff}} - T_0$ as a function of M_1 (T_0 is the effective temperature of the reference spherical model of a star with mass M_1 at $d \to \infty$). This comparison fully extracts only the effect of tidal deformation. The different, color-coded curves are now for

different d values. For M_1 in the 1 M$_\odot$ to 1.6 M$_\odot$ range, the changes of effective temperature with d are suppressed and stay quite small.

There is a significant feature around 1.2 M$_\odot$, where the temperatures experience a jump. The larger the fill-out factor, the more significant the jump is. This phenomenon is closely related to the Kraft break mentioned and thoroughly discussed in section 4.6.1.

4.5   Additional analysis for $q = 0.1$ and $q = 1$

A less detailed analysis has been conducted for mass ratios q which represent the endpoints of the observed range of contact binary systems. Although most of contact binaries have been observed to have $q \simeq 0.3$, their observed values range from $\simeq 0.1$ to unity [theoretically, the q values could be as small as 0.03, Pešta and Pejcha, 2022, but it is not clear whether they would be observationally detectable]. At this moment, we use $q = 0.1$ and $q = 1$ cases.

In Figs. 4.9, the effective temperatures for models with different separations are shown in systems with mass ratio 0.1. Although the relation roughly follows the one for more standard mass ratio (Fig. 4.6)), the correlation between the fill-out factor and effective temperature for contact configuration systems is much less clear. First, the temperature drop at the inner critical configuration is smaller ($\simeq 300$ K here). Second, for fill-out factors larger than 1.5, the temperature attains a value basically equal to that of a spherical star of the same mass. In fact, both may be expected, since the secondary is small compared to the primary and does not deform the geometry much.

In Figs. 4.10, the effective temperatures for models with different separations are shown in systems with mass ratio 1, i.e., two equal solar mass stars. Here the temperatures of models in the common envelope configuration exhibit very different behavior. Beyond the inner critical configuration, the effective temperature appears to be approximately constant. We do not have a simple explanation of this behavior, but the geometry of the surface layers is the most extreme of the studied cases and the correction factors f_p and f_T most severely deviate from unity (see Figs. 2.5 and 2.4). We also recall that the luminosity of the companion star is not added to our solution, which may be the most serious drawback in the equal-mass ($q = 1$) case. So in reality, T_{eff} may be increasing towards the outer critical configuration. We also noted that in these more extreme mass ratios (discussed in this Section), the models are generally less stable and undergo a kind of oscillations of the TRO type. For this reason, models of contact systems near critical configurations should be taken with caution.

In order to show that the comparison in the next section is consistent for all mass ratios that are observed. For every situation, the temperature correlated positively with the fill-out factor in contact configurations. For a constant fill-out factor in the common envelope, it seems that there is a negative correlation between the effective temperature of the primary with the mass ratio of the system. This relation is discussed in the next sections of this chapter.
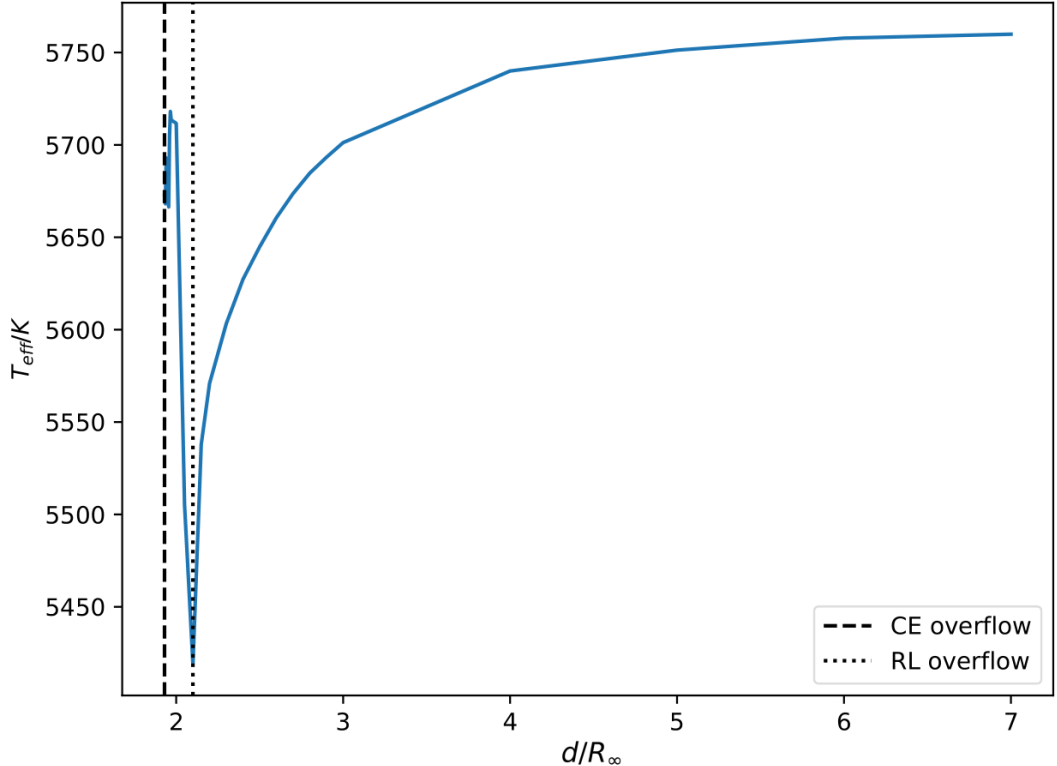
Figure 4.9: The effective temperature as a function of the separation d of the two stars (normalized to the radius R_∞ of a non-deformed, isolated star) is plotted for systems with mass ratio $q = 0.1$ and $M_1 = 1\ \mathrm{M_\odot}$. The onset of the two key configurations - the Roche lobe overflow and the common envelope overflow - are shown with dotted and dashed lines respectively. Note the rapid drop of the effective temperature as soon as the mass starts to overflow the Roche lobe. In this case, however, the common envelope configurations with the fill-out factor ≥ 1.5 have their effective temperature resembling that of the asymptotic value corresponding to the isolated primary.

4.6 Observational connections

While this thesis serves mainly as a proof of concept of the new method of modelling tidally deformed stars, we mentioned already in the introduction that ideally we also aim at making some connections with recent observational data. This motivation is explored more thoroughly in this section.

4.6.1 Connection to Kraft break and ASSASN survey data

The recent paper by Jayasinghe et al. [2020] presented an analysis of W UMa type contact binaries using All Sky Automated Survey for SuperNovae (ASSASN), complementing them with archival data from Gaia, 2MASS, AllWISE, LAMOST, GALAH, RAVE, and APOGEE surveys. The final set of about 71200 systems included over 12000 new discoveries and represents the most extensive compilation so far.

While studying different aspects of the sample of contact binaries, a clear
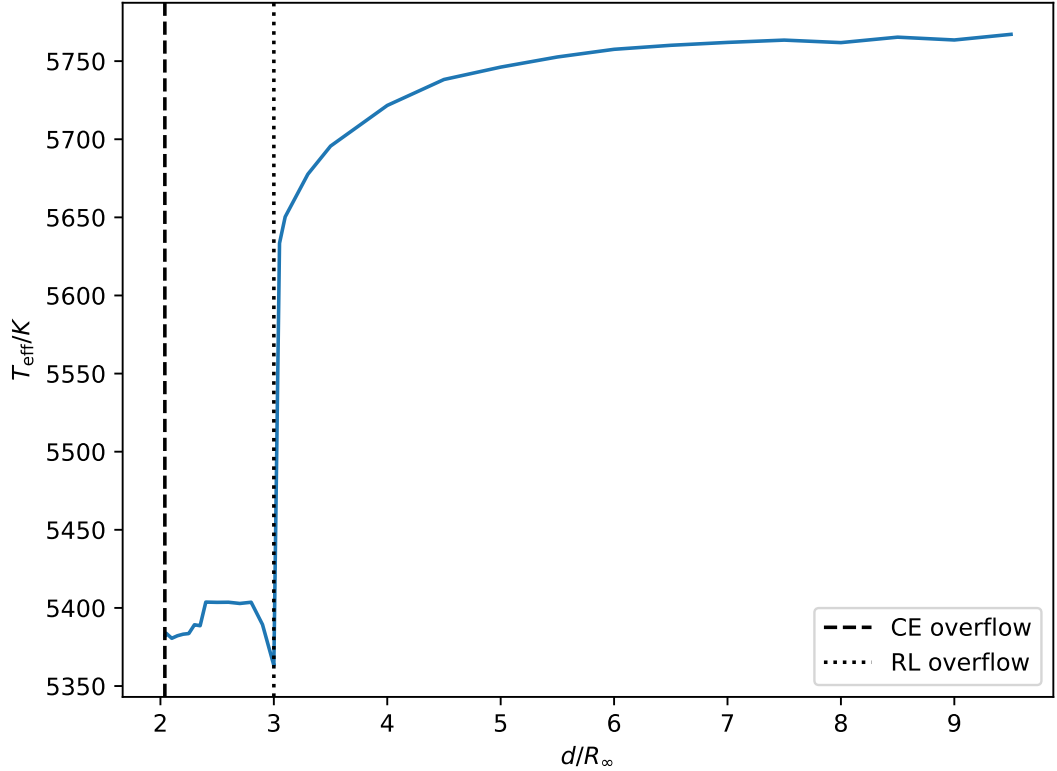
Figure 4.10: The effective temperature as a function of the separation d of the two stars (normalized to the radius R_∞ of a non-deformed, isolated star) is plotted for systems with mass ratio $q = 1$ and $M_1 = 1\ \mathrm{M_\odot}$. The onset of the two key configurations - the Roche lobe overflow and the common envelope overflow - are shown with dotted and dashed lines respectively. Note the rapid drop of the effective temperature as soon as the mass starts to overflow the Roche lobe. In this case, however, in the common envelope configuration phase, the temperature stagnates at about the same level.

dichotomy was noted in the effective temperature T_{eff} (in K) vs orbital period P (in d) space. The approximate line described by

$$T_{\mathrm{eff}} = 6710 - 1760\log(P/0.5),\qquad(4.6)$$

separates the two populations. The hotter population has a systematically longer period, whereas the opposite trend is observed for the colder population (we will follow the nomenclature of the paper and call the hotter population the early type population and the cooler population the late type population.). The authors argue that Eq. (4.6) provides a much clearer distinction between early and late type systems than the criterion based on the period P (in d)

$$\log P = -0.25,\qquad(4.7)$$

which has been traditionally used in the literature.

It has also been conjectured that the dichotomy is caused by effects related to the Kraft break - the abrupt spindown in stellar rotation at about 6200 K. This break is commonly explained by magnetic dynamos operating in the upper

stellar layers and allowing to transfer rotational angular momentum to winds in a process commonly referred to as magnetic braking [e.g., Matt et al., 2012]. In the case of main sequence single (isolated) massive and hot stars do not have deep convective envelopes, so the magnetic braking process is inefficient, and indeed they are observed to rotate fast. On the contrary, low mass and cooler stars develop a significant subsurface convective layer and their rotation is slow (recall the case of the Sun). Even though this hypothesis is based on an order of magnitude calculations and is still being developed towards a more rigorous model, it is by far the leading explanation of the Kraft break. From the observational side, El-Badry et al. [2022] found evidence of the saturation of magnetic fields and confirmed magnetic braking predictions for new models where the torque is inversely proportional to the period, by looking at the distribution of periods for eclipsing binaries.

However, the way how the mechanism works in contact binary systems is more of a mystery. Note that the picture provided by observations is actually reversed: the hotter systems tend to have longer orbital periods, while the cooler systems tend to have shorter orbital periods. The intriguing point is that the division occurs at about the same effective temperature of 6200 K. As in the case of single stars, a thorough (possibly 3D magnetohydrodynamic) model would be necessary to account for all the complex processes, including the magnetized winds escaping from the systems. However, the simple models developed in this thesis could at least shed some light on the principal parameters that could eventually point in the direction of the resolution of the problem.

In this thesis, we do not include modelling of the stellar wind. A fundamental parameter allowing the magnetic dynamo to operate and to promote the magnetic breaking process is, however, the depth of the surface convective layer. We observed that in all tidally deformed models, the thickness of this layer increased when compared to their spherical counterparts. The thickness also increased when the orbital period of the binary decreased (i.e., the two components were put closer to each other), and therefore the fill-out factor of the contact binary increased. If confirmed by more complex models, this effect could point to magnetic braking having an even stronger effect in contact binaries. That being said, many other parameters come into play, such as very different and anisotropic mass loss of contact binaries. This means that even with thicker convective layers, the overall braking effect could be smaller. Unfortunately, its estimates in theoretical models are still quite uncertain, and without them, the debate cannot be concluded.

Regardless of the specific mechanism, the tidal deformation effect alone showed a feature similar to the temperature gap from Jayasinghe et al. [2020]. In Fig. 4.8, the feature around $1.2 \, M_\odot$ could represent the sudden increase in temperature corresponding to the gap.

An interesting prediction of models developed in this thesis is the relation between the fill-out factor and effective temperature described in Sections 4.4 and 4.5.

4.6.2   Observational evidence about fill-out factors of contact binaries

Regarding efforts to get as complete parameters of contact binary systems as possible from the observations, studies as Yakut and Eggleton [2005] attempted to combine a wide range of data. However, a typical problem was the data inhomogeneity, mainly due to the various instrumental accuracy. As a result, these works did not reach convincing and justifiable conclusions.

Luckily, powerful modern survey programs in astronomy have changed the game over the past decade or so. As an example, Kobulnicky et al. [2022] conducted a Bayesian analysis of close binary parameters from the Kepler survey. Light curves were fitted with a model accounting for the main system parameters - the period, the derivative of the period, orbital inclination, mass ratio, fill-out factor, and the ratio of the individual temperatures. Observed objects were classified by several parameters into detached, contact, and ambiguous models. In order to be considered contact systems, the root mean square error of a contact configuration model had to be less than 0.005 (and smaller than that of any detached model), and the radius of either star had to be larger than 95% of the Roche lobe radius appropriate to the respective Roche potential. Out of the 783 total objects, these criteria yielded 173 probable contact systems, 114 probable detached systems, and 491 ambiguous systems. One of the fitted parameters in their work was the fill-out factor F (Eq. (2.17)), an important parameter in our models. Interestingly, Kobulnicky et al. [2022] missed to correlate their results with F, yet we argue below it may potentially lead to surprising results. In particular, we split the stars into populations below and above the Kraft break, approximately below and above the effective temperature of 6200 K. We then analyzed the fill-out factor in each of these categories separately. Due to a small sample of sure contact configurations, the ambiguous category was also considered, as many systems are probable contact systems only with a slightly smaller degree of certainty. In Fig. 4.11 differential and cumulative distributions of F for both populations are displayed and compared to each other.

We can see that contact binaries in the second (hotter) population have systematically larger fill-out factors than those in the first (cooler) population (having median values of F equal to ~ 0.7 and ~ 0.47, respectively). This discrepancy has been pointed towards before by Mochnacki [1981]. Furthermore, about 20% of the systems from the second population have a very large fill-out factor - over 1.9. We should, however, admit that this result is partly suspicious and may not be accurate, since a large mass loss starts occurring well before the common envelope is filled up to these values. Among others, Ruciński [1973] predicts that the average fill-out should be around 1.25. However, we do not have tools to verify and/or improve these results.

To quantify the significance of the difference in cumulative distributions shown in Fig. 4.11, the Kolmogorov-Smirnov test was used. This is a standard statistical method applied to determine whether the two cumulative sets of data are drawn from the same probability distribution or not. This method gave a statistical value of 0.180 and a p-value of 2.56×10^{-4} of the null hypothesis, rejecting thus similarity of the two distributions.

Another interesting result from the work of Kobulnicky et al. [2022] concerns
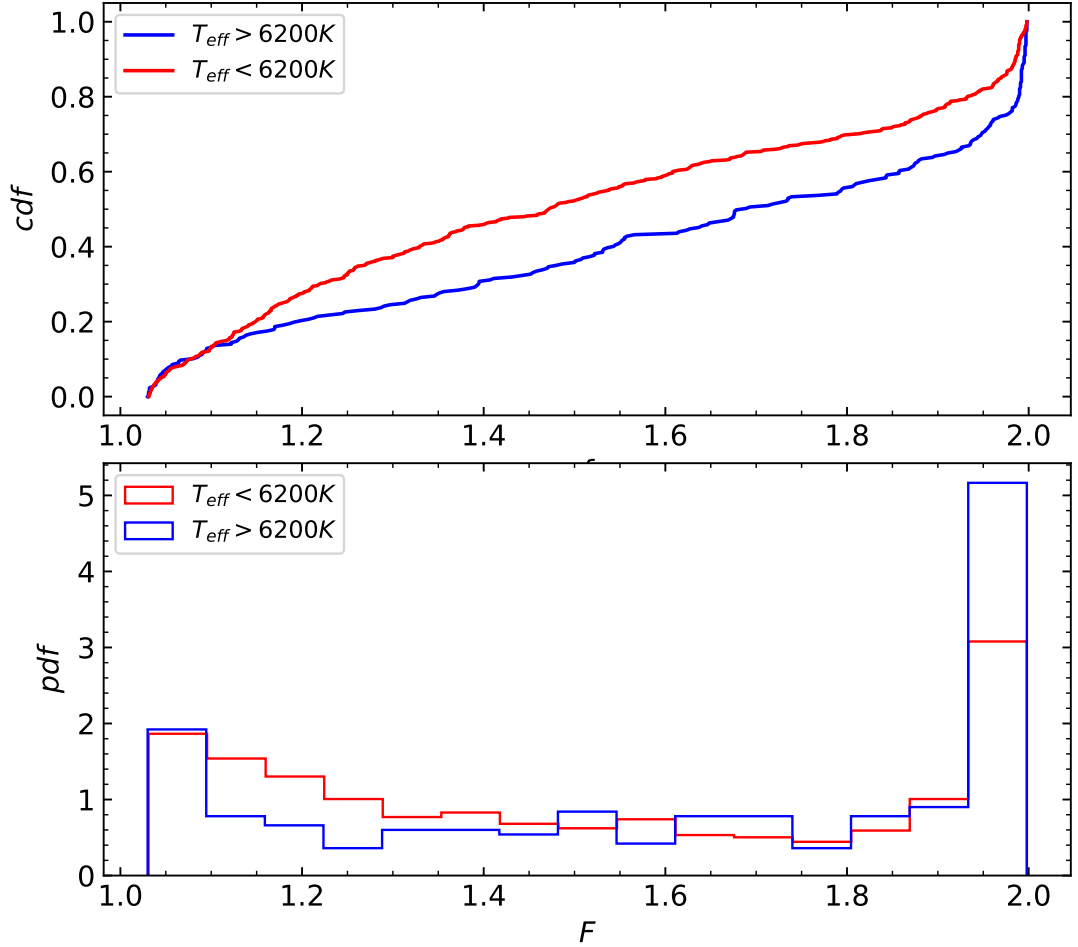
Figure 4.11: Cumulative (cdf, top) and differential (pdf, bottom) probability density distribution function of the fill-out factor of the early type (blue) and late type (red) populations of Kepler contact binaries. Kolmogorov-Smirnov test on the cumulative functions hints the two sets are not drawn from the same probability distribution.

the typical mass ratio q of the contact binaries. Dividing the sample again into the early and late type contact binaries, Fig. 4.12 shows the probability density distribution of q for the two groups separately. Clearly, a typical value for the early type binaries is smaller (median q about 0.31) than that of the late type binaries (median q about 0.435). Pešta and Pejcha [2022] predicts a similar dichotomy in median mass ratios for the warmer versus colder stellar populations, however, the actual predicted distribution is very different, and much less flat. Combined with the finding of section 4.5, this discrepancy could also play a role in the gap observed from Jayasinghe et al. [2020].

We should, however, caution the reader that these results do not represent a rigorous analysis and thus no hasty conclusions should be made. They should be taken simply as an interesting direction of thought for further, more complex modeling of contact binary systems.
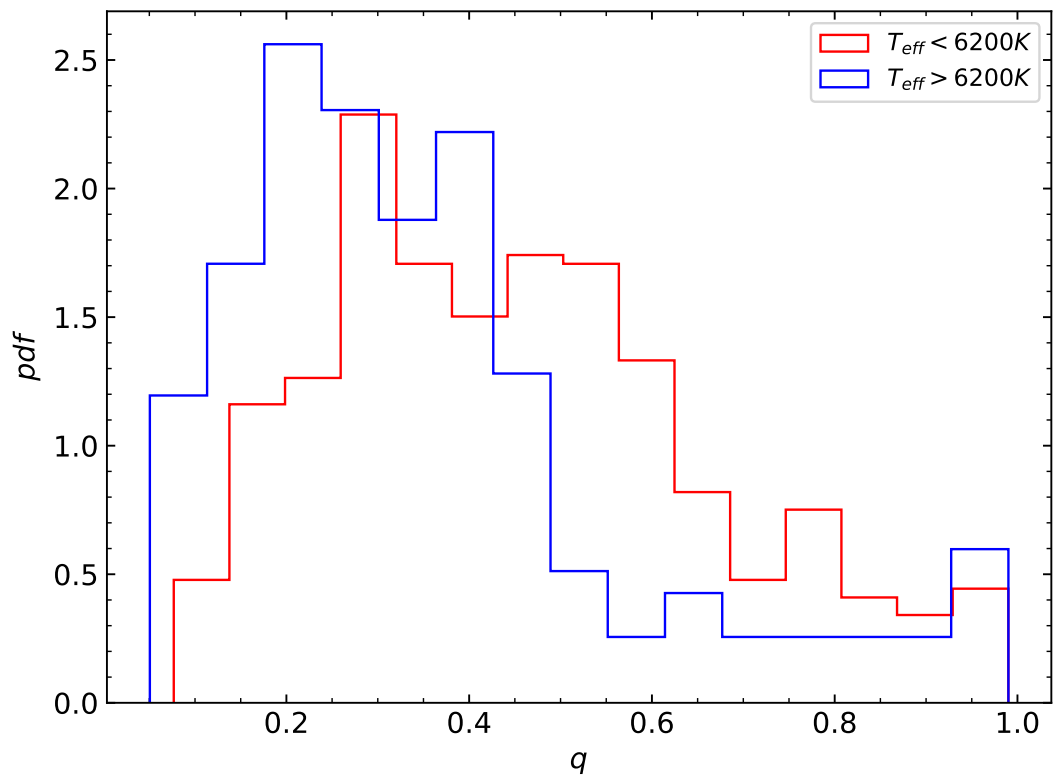
Figure 4.12: Probability density distribution of the mass ratio q for the early type (blue) and late type (red) populations of Kepler contact binaries. The early type systems seem to have systematically smaller q values.

5. Discussions

In this chapter, possible extensions of the model presented in this Thesis are discussed, alongside of interesting applications in seemingly unrelated directions.

5.1 Possible application to binary interaction in classical novae

The application of our model could be extended towards other astrophysical phenomena where a common envelope forms and the interaction with the secondary is limited mainly towards the effects of tidal deformation. A good example of this situation is the binary interaction phase before classical novae. This is a situation when a main sequence star or a red giant and a white dwarf orbit in a binary system close enough so that matter starts accreting on the white dwarf. This creates an atmosphere that gets heated by the white dwarf and rapidly expands encircling the other star. For a more thorough review of the topic, see Bode and Evans [2008]. Effectively, plasma with very different entropies does not interact, so this model could be used to model hot flow around the main sequence star, as this envelope has significantly higher entropy than the star. The star effectively acts as a hole analogously to the secondary in our work above.

Shen and Quataert [2022] found that most of the mass loss happens within binary evolution and that this interaction phase can last much longer than was previously expected. Only after the region of acceleration recedes within the Roche lobe radius of the white dwarf. Modelling this phase is crucial to create population synthesis estimates for novae rates.

5.2 Analogy with effects in massive star evolution

In this thesis, only low-mass binaries were explored. Massive stars can have completely different structure due to different physical phenomena in action, and this could also have interesting implications for the behaviour of massive contact configurations. As mentioned in Sec. 2.4, there are only 12 contact binaries observed with masses over 15 $M_\odot$. Available models suggest that a much greater fraction of massive short-period binaries evolve to a contact phase than low mass W UMa systems.

An interesting aspect of massive stars is the possibility of enhanced opacity due to iron (or iron-group) atoms in the upper layers of the atmosphere. This may lead to the formation of a small surface convective layer, analogous to the one present in low mass stars (Chapter 4). Recall that the tidal interaction explored in this Thesis significantly altered the parameters of the surface layer, and it would be interesting to understand this behaviour in massive stars. In a paper, Jiang et al. [2015], interesting behaviour of convective and radiative zones around the iron peak was found, alongside oscillatory behaviours. These oscillations could be somewhat analogical to TRO oscillations mentioned in chapter 1.

5.3 Future work

Exploring the range of massive stars would be an interesting direction to follow, as discussed in the previous section.

Understanding the limitations of our approach in modelling the structure of the contact binaries is an important task for future work. The 1D approximation is definitely not sufficient to make fully accurate predictions about contact binary systems due to the absence of symmetry compared to single stars. Ultimately, full 3D magneto-hydrodynamical simulations will be needed to grasp all effects.

The models presented in this Thesis deal only with the tidal deformation (geometric) aspects of the problem. Still, introducing the corresponding correction factors into the equations of stellar structure, even some physical features (such as the presence and location of the convective layers) were changed. The next step, still within the 1D approach, might be to implement the effects of the secondary more fully. For instance, one could imagine estimating and implementing the radiative energy flux at the secondary Roche lobe contributing to the structure of the primary. Intuitively, this would be especially important for systems with sizeable secondaries, namely when q is close to unity. The luminosity of the secondary then basically equals that of the primary, and so far our models are missing this contribution. One may wonder how this change would modify the structure of the common envelope.

There are many effects of binary systems and of stellar evolution in general, that are not considered in this model. Mass transfer seems to play a key role in contact binary stellar evolution, as well as in the stability of stationary configurations. The models developed in this thesis are not well suited for mass transfer, as the boundary between stars is the whole secondary Roche lobe. Boundary conditions at the critical equipotential could be defined to dynamically vary the mass ratio of the system. Alongside mass transfer, energy transfer has to also play a key role in the evolution and stability of contact binaries. The increased thickness of the convective surface layer in our models could hint at larger meridional flows around the binary as predicted by Kahler, or some different mixing effects in the common envelope distributing energy so that the ratio of the temperatures of the two components stays close to unity. A different approach will be taken by Fabry et al. [2022], whose way of separating the two stars in the contact binary system is very well suited for energy transfer between the two stars with simple boundary conditions.

The aim of this Thesis was only to construct thermally and hydrostatically stationary models. A natural step further is stellar evolution. On nuclear timescales, the integrated effects of the phenomena mentioned in the paragraphs above could change the model completely. Nuclear evolution changes the chemical composition of the star significantly, which would have to be taken into account, as well as the evolution changes in secondary. This could be done for example by varying the boundary conditions at the critical equipotential in time by either only some preset conditions, or through more advanced dynamical modelling depending on the boundary parameters.

Regarding the observational comparisons - to make bolder claims and to explain observational data around the Kraft break, winds and a model of magnetic braking would be needed as discussed in section 4.6.1.

Conclusions

Recently, observations of contact binary stars from Jayasinghe et al. [2020] showed a clear dichotomy with a gap between two populations in effective temperatures. In this thesis, new models of these systems are created to explain this gap.

The Kippenhahn averaging formalism was successfully applied to the Roche potential and used to formulate approximate models of tidally deformed primaries in close binary systems. The models were constructed by modifying classical stellar structure equations with correction factors due to the geometry of tidal effects. These correction factors were obtained by generating large tables of integrated quantities of the Roche potential. Effectively, the contact binary is a single significantly deformed star tidally deformed by a point mass creating a notional hole inside the star.

We considered both the detached and the contact configurations. These tidally deformed models are thermally stable if chemical composition evolution is neglected. We explored the parametric dependence of the results on three quantities: mass ratio q in the binary, surface equipotential C of the primary (or the fill-out factor $F(C)$), and mass M_1 of the primary.

In all models of tidally deformed stars, the deformation lowered the effective temperature of the star in comparison with the spherical counterpart. For detached configurations, this effect is increased with increasing fill-out up towards Roche lobe overflow.

For contact configurations, models developed in this thesis predicted a positive correlation of temperature with the fill-out factor all the way to common envelope overflow. This coincides with a similar trend obtained from processing observational data from Kobulnicky et al. [2022]. Here, fill-out factors were compared for the two distinct populations from Kobulnicky et al. [2022]. This analysis shows that the second population has a systematically higher fill-out factor, which could lead to a systematically higher temperature.

Another finding from models is the correlation between the mass ratio and the tidal deformation effect on temperature (and therefore smaller temperature). Small mass ratio contact binaries are closer to their spherical counterparts than systems with mass ratios close to 1. This means that the tidal effect on temperature is smaller. The effect was only tested on three mass ratios, more tests would be needed for more direct conclusions. The findings from observational data show a systematic difference in the mass ratio of the two populations.

Finally, when isolating the effect of tidal deformation, we saw a jump in temperatures around 1.2 $M_\odot$ for most fill-out factors, most pronounced for fill-out factors around Roche lobe overflow.

The three effects mentioned in the last three paragraphs successfully reproduced, on a qualitative level, the gap described by Jayasinghe et al. [2020].

In all models, the thickness of the surface convective layer present in low mass stars increased with increasing tidal deformation, with the greatest increase happening when overflowing its Roche lobe. The cause is found to be a significant increase in opacity in this reason due to deformation effects. This layer seems to play a key role in the complete quantitative explanation of the effects found in the models developed in this thesis.

Full 3D magnetohydrodynamic models would be needed for a complete description of the functioning of contact binary stars. However, even simple models like those developed in this thesis can point in the directions of interesting phenomena in such complex systems as contact binary stars.

Bibliography

LA Almeida, Hugues Sana, SE De Mink, F Tramper, I Soszyn, N Langer, RH Barbá, M Cantiello, A Damineli, Alex de Koter, et al. Discovery of the massive overcontact binary vfts 352: evidence for enhanced internal mixing. *The Astrophysical Journal*, 812(2):102, 2015.

Sarbani Basu, MH Pinsonneault, and John N Bahcall. How much do helioseismological inferences depend on the assumed reference model? *The Astrophysical Journal*, 529(2):1084, 2000.

L Binnendijk. The orbital elements of w ursae majoris systems. *vistas in Astronomy*, 12:217–256, 1970.

Michael F Bode and Aneurin Evans. Classical novae. *Classical Novae*, 43, 2008.

T Borkovits, MM Elkhateeb, Sz Csizmadia, J Nuspl, IB Bíró, T Hegedüs, and R Csorvási. Indirect evidence for short period magnetic cycles in w uma stars-period analysis of five overcontact systems. *Astronomy & Astrophysics*, 441(3): 1087–1097, 2005.

S. Cassisi, A. Y. Potekhin, A. Pietrinferni, M. Catelan, and M. Salaris. Updated Electron-Conduction Opacities: The Impact on Low-Mass Stellar Models. , 661 (2):1094–1104, June 2007. doi: 10.1086/516819.

J. P. Cox and R. T. Giuli. *Principles of stellar structure.* 1968.

Donát R Czavalinga, Tibor Mitnyan, Saul A Rappaport, Tamás Borkovits, Robert Gagliano, Mark Omohundro, Martti HK Kristiansen, and András Pál. Newly identified compact hierarchical triple system candidates using gaia dr3. *arXiv preprint arXiv:2212.02903*, 2022.

Olin J Eggen. Contact binaries, ii. *Memoirs of the Royal Astronomical Society*, 70:111, 1967.

P. P. Eggleton. Aproximations to the radii of Roche lobes. , 268:368–369, May 1983. doi: 10.1086/160960.

Peter Eggleton. Theories of contact binary stars. In *2nd cambridge workshop on cool stars, Stellar Systems and the Sun*, volume II. Cambridge University Press, 1982.

Peter Eggleton. *Evolutionary processes in binary and multiple stars*, volume 40. Cambridge University Press, 2006.

Kareem El-Badry, Charlie Conroy, Jim Fuller, Rocio Kiman, Jan van Roestel, Antonio C Rodriguez, and Kevin B Burdge. Magnetic braking saturates: evidence from the orbital period distribution of low-mass detached eclipsing binaries from ztf. *Monthly Notices of the Royal Astronomical Society*, 517(4): 4916–4939, 2022.

AS Endal and S Sofia. The evolution of rotating stars. 1: Method and exploratory calculations for a 7 solar mass star. Technical report, 1976.

M Fabry, P Marchant, and H Sana. Modeling overcontact binaries-i. the effect of tidal deformation. *Astronomy & Astrophysics*, 661:A123, 2022.

J Faulkner, IW Roxburgh, and PA Strittmatter. Uniformly rotating main-sequence stars. *The Astrophysical Journal*, 151:203, 1968.

Jason W Ferguson, David R Alexander, France Allard, Travis Barman, Julia G Bodnarik, Peter H Hauschildt, Amanda Heffner-Wong, and Akemi Tamanai. Low-temperature opacities. *The Astrophysical Journal*, 623(1):585, 2005.

M. Y. Fujimoto. The Evolution of Accreting Stars with Turbulent Mixing. *The Astrophysical Journal*, 419:768, December 1993. doi: 10.1086/173528.

J Hazlehurst. The equilibrium of a contact binary. *Astronomy and Astrophysics*, 271:209, 1993.

J Hazlehurst. On the cyclic contact-binary theory. *The Observatory*, 121:86–91, 2001.

John Hazlehurst. The nature of contact binaries. *Monthly Notices of the Royal Astronomical Society*, 149(2):129–146, 1970.

Carlos A. Iglesias and Forrest J. Rogers. Updated Opal Opacities. , 464:943, June 1996. doi: 10.1086/177381.

N Ivanova, S Justham, X Chen, O De Marco, CL Fryer, E Gaburov, H Ge, E Glebbeek, Z Han, X-D Li, et al. Common envelope evolution: where we stand and how we can move forward. *The Astronomy and Astrophysics Review*, 21(1): 1–73, 2013.

T Jayasinghe, KZ Stanek, CS Kochanek, BJ Shappee, MH Pinsonneault, T WS Holoien, Todd A Thompson, JL Prieto, M Pawlak, O Pejcha, et al. The asas-sn catalogue of variable stars–vii. contact binaries are different above and below the kraft break. *Monthly Notices of the Royal Astronomical Society*, 493(3): 4045–4057, 2020.

Adam S. Jermyn, Josiah Schwab, Evan Bauer, F. X. Timmes, and Alexander Y. Potekhin. Skye: A Differentiable Equation of State. , 913(1):72, May 2021. doi: 10.3847/1538-4357/abf48e.

Yan-Fei Jiang, Matteo Cantiello, Lars Bildsten, Eliot Quataert, and Omer Blaes. Local radiation hydrodynamic simulations of massive star envelopes at the iron opacity peak. *The Astrophysical Journal*, 813(1):74, 2015.

H Kähler. A self-consistent treatment of the mechanical structure of contact binaries. *Astronomy and Astrophysics*, 157:329–334, 1986.

H Kähler. On the structure of contact binaries. *Astronomy & Astrophysics*, 395 (3):907–913, 2002a.

H Kähler. The structure equations of contact binaries. *Astronomy & Astrophysics*, 395(3):899–905, 2002b.

H Kähler. The structure of contact binaries. *Astronomy & Astrophysics*, 414(1): 317–333, 2004.

R Kippenhahn and H-C Thomas. A simple method for the solution of the stellar structure equations including rotation and tidal forces. In *International Astronomical Union Colloquium*, volume 4, pages 20–29. Cambridge University Press, 1970.

Henry A Kobulnicky, Lawrence A Molnar, Evan M Cook, and Lauren E Henderson. A bayesian analysis of physical parameters for 783 kepler close binaries: Extreme-mass-ratio systems and a new mass ratio versus period lower limit. *arXiv preprint arXiv:2202.01187*, 2022.

Zdenek Kopal. *Close binary systems*. 1959.

Gerard P Kuiper. On the interpretation of beta lyrae and other close binaries. *The Astrophysical Journal*, 93:133, 1941.

Olivera Latković, Atila Čeki, and Sanja Lazarević. Statistics of 700 individually studied w uma stars. *The Astrophysical Journal Supplement Series*, 254(1):10, 2021.

Denis A. Leahy and Janet C. Leahy. A calculator for Roche lobe properties. *Computational Astrophysics and Cosmology*, 2:4, May 2015. doi: 10.1186/s40668-015-0008-8.

P. Ledoux. Stellar Models with Convection and with Discontinuity of the Mean Molecular Weight. *The Astrophysical Journal*, 105:305, March 1947. doi: 10.1086/144905.

Kai Li, Qi-Qi Xia, Chun-Hwey Kim, Shao-Ming Hu, Di-Fu Guo, Min-Ji Jeong, Xu Chen, and Dong-Yang Gao. Two contact binaries with mass ratios close to the minimum mass ratio. *The Astrophysical Journal*, 922(2):122, 2021.

Lifang Li, Zhanwen Han, and Fenghui Zhang. Structure and evolution of low-mass w uma-type systems. *Monthly Notices of the Royal Astronomical Society*, 351 (1):137–146, 2004.

Stephen H Lubow and Frank H Shu. On the structure of contact binaries. iv-high-mass models. *The Astrophysical Journal*, 229:657–660, 1979.

LB Lucy. The structure of contact binaries. *The Astrophysical Journal*, 151:1123, 1968.

LB Lucy. W ursae majoris systems with marginal contact. *The Astrophysical Journal*, 205:208–216, 1976.

John C Lurie, Karl Vyhmeister, Suzanne L Hawley, Jamel Adilia, Andrea Chen, James RA Davenport, Mario Jurić, Michael Puig-Holzman, and Kolby L Weisenburger. Tidal synchronization and differential rotation of kepler eclipsing binaries. *The Astronomical Journal*, 154(6):250, 2017.

Pablo Marchant, Kaliroë MW Pappas, Monica Gallegos-Garcia, Christopher PL Berry, Ronald E Taam, Vicky Kalogera, and Philipp Podsiadlowski. The role of mass transfer and common envelope evolution in the formation of merging binary black holes. *Astronomy & Astrophysics*, 650:A107, 2021.

Sean P Matt, Keith B MacGregor, Marc H Pinsonneault, and Thomas P Greene. Magnetic braking formulation for sun-like stars: dependence on dipole field strength and rotation rate. *The Astrophysical Journal Letters*, 754(2):L26, 2012.

Søren Meibom, Robert D Mathieu, and Keivan G Stassun. An observational study of tidal synchronization in solar-type binary stars in the open clusters m35 and m34. *The Astrophysical Journal*, 653(1):621, 2006.

LTS Mendes, F D'Antona, and I Mazzitelli. Theoretical models of low-mass, pre-main sequence rotating stars. i. the effects on lithium depletion. *Astronomy and Astrophysics*, 341:174–180, 1999.

E Meyer-Hofmeister. Loops in the hr diagram during core hellum˜ burning and the effect of rotation. *Astronomy and Astrophysics*, 16:282, 1972.

G. Meynet and A. Maeder. Stellar evolution with rotation. I. The computational method and the inhibiting effect of the μ-gradient. *Astronomy & Astrophysics*, 321:465–476, May 1997.

STEFAN W Mochnacki. Contact binary stars. *The Astrophysical Journal*, 245: 650–670, 1981.

SW Mochnacki. Accurate integrations of the roche model. *The Astrophysical Journal Supplement Series*, 55:551–561, 1984.

N. Morgan, M. Sauer, and E. Guinan. New Light Curves and Period Study of the Contact Binary W Ursae Majoris. *Information Bulletin on Variable Stars*, 4517:1, September 1997.

DL Moss and JAJ Whelan. The structure of w ursae majoris systems. *Monthly Notices of the Royal Astronomical Society*, 149(2):147–165, 1970.

Yoji Osaki. Mass-luminosity relationship in close binary systems of w ursae majoris type. *Publications of the Astronomical Society of Japan*, 17:97, 1965.

B. Paczyński, D. M. Szczygieł, B. Pilecki, and G. Pojmański. Eclipsing binaries in the All Sky Automated Survey catalogue. *Monthly Notices of the Royal Astronomical Society*, 368(3):1311–1318, April 2006. doi: 10.1111/j.1365-2966.2006.10223.x.

Bill Paxton, Lars Bildsten, Aaron Dotter, Falk Herwig, Pierre Lesaffre, and Frank Timmes. Modules for experiments in stellar astrophysics (mesa). *The Astrophysical Journal Supplement Series*, 192(1):3, 2010.

Bill Paxton, R Smolec, Josiah Schwab, A Gautschy, Lars Bildsten, Matteo Cantiello, Aaron Dotter, R Farmer, Jared A Goldberg, Adam S Jermyn, et al. Modules for experiments in stellar astrophysics (mesa): pulsating variable stars, rotation, convective boundaries, and energy conservation. *The Astrophysical Journal Supplement Series*, 243(1):10, 2019.

Milan Pešta and Ondřej Pejcha. Mass-ratio distribution of contact binary stars. *arXiv preprint arXiv:2212.02553*, 2022.

Robert Piessens, Elise de Doncker-Kapenga, Christoph W Überhuber, and David K Kahaner. *Quadpack: a subroutine package for automatic integration*, volume 1. Springer Science & Business Media, 2012.

M. H. Pinsonneault, Steven D. Kawaler, S. Sofia, and P. Demarque. Evolutionary Models of the Rotating Sun. *The Astrophysical Journal*, 338:424, March 1989. doi: 10.1086/167210.

A. Y. Potekhin and G. Chabrier. Thermodynamic Functions of Dense Plasmas: Analytic Approximations for Astrophysical Applications. *Contributions to Plasma Physics*, 50(1):82–87, January 2010. doi: 10.1002/ctpp.201010017.

Adrian T Potter, Christopher A Tout, and John J Eldridge. Towards a unified model of stellar rotation. *Monthly Notices of the Royal Astronomical Society*, 419(1):748–759, 2012.

J Alistair Robertson and Peter P Eggleton. The evolution of w ursae majoris systems. *Monthly Notices of the Royal Astronomical Society*, 179(3):359–375, 1977.

Édouard Roche. *Essai sur la constitution et l'origine du systeme solaire*. Gauthier-Villars, 1873.

F. J. Rogers and A. Nayfonov. Updated and Expanded OPAL Equation-of-State Tables: Implications for Helioseismology. , 576(2):1064–1074, September 2002. doi: 10.1086/341894.

S. M. Ruciński. The W UMa-type Systems as Contact Binaries. I. Two Methods of Geometrical Elements Determination. Degree of Contact. , 23:79, January 1973.

Slavek M. Rucinski. Time Sequence Spectroscopy of AW UMa. The 518 nm Mg i Triplet Region Analyzed With Broadening Functions. *The Astrophysical Journal*, 149(2):49, February 2015. doi: 10.1088/0004-6256/149/2/49.

SM Rucinski. Contact binaries of the w uma type. In *The Realm of Interacting Binary Stars*, pages 111–142. Springer, 1993.

George B Rybicki and Alan P Lightman. Radiative processes in astrophysics. originally published, 2004.

Ken J Shen and Eliot Quataert. Binary interaction dominates mass ejection in classical novae. *arXiv preprint arXiv:2205.06283*, 2022.

F. H. Shu, S. H. Lubow, and L. Anderson. On the structure of contact binaries. III. Mass and energy flow. , 229:223–241, April 1979. doi: 10.1086/156948.

Frank H Shu. Theories of contact binary stars. In *Symposium-International Astronomical Union*, volume 88, pages 477–484. Cambridge University Press, 1980.

Frank H Shu, Stephen H Lubow, and Lawrence Anderson. On the structure of contact binaries. i-the contact discontinuity. *The Astrophysical Journal*, 209: 536–546, 1976.

Frank H Shu, Stephen H Lubow, and Lawrence Anderson. On various criticisms of the contact discontinuity model. *The Astrophysical Journal*, 239:937–940, 1980.

Brian L Smith. The structure of rotating stars from an extension of the kippenhahn-thomas method. *Astrophysics and Space Science*, 25(1):195–205, 1973.

David H Smith, J Alistair Robertson, and Robert Connon Smith. On internal inconsistencies in the discontinuity model for contact binary stars. *Monthly Notices of the Royal Astronomical Society*, 190:177–183, 1980.

K Stepien. Evolutionary status of late-type contact binaries. *arXiv preprint astro-ph/0510464*, 2005.

K Stępień. Large-scale circulations and energy transport in contact binaries. *Monthly Notices of the Royal Astronomical Society*, 397(2):857–867, 2009.

Weijia Sun, Xiaodian Chen, Licai Deng, and Richard de Grijs. Physical parameters of late-type contact binaries in the northern catalina sky survey. *The Astrophysical Journal Supplement Series*, 247(2):50, 2020.

Victor Szebehely. *Theory of orbits. The restricted problem of three bodies.* 1967.

Joseph S. Tenn. Keepers of the double stars. *Journal of Astronomical History and Heritage*, 16(1):81–93, March 2013.

F. X. Timmes and F. Douglas Swesty. The Accuracy, Consistency, and Speed of an Electron-Positron Equation of State Based on Table Interpolation of the Helmholtz Free Energy. , 126(2):501–516, February 2000. doi: 10.1086/313304.

H Von Zeipel. The radiative equilibrium of a rotating system of gaseous masses. *Monthly Notices of the Royal Astronomical Society*, 84:665–683, 1924.

JAJ Whelan. Contact binary systems: Why the secondary might be hotter. *Monthly Notices of the Royal Astronomical Society*, 156(1):115–128, 1972.

RE Wilson. On the a-type w ursae majoris systems. *The Astrophysical Journal*, 224:885–891, 1978.

Kadri Yakut and Peter P Eggleton. Evolution of close binary systems. *The Astrophysical Journal*, 629(2):1055, 2005.

WM Yang and SL Bi. Angular momentum transport and element mixing in the stellar interior-i. application to the rotating sun. *Astronomy & Astrophysics*, 449(3):1161–1168, 2006.

J-P Zahn. Tidal evolution of close binary stars. i-revisiting the theory of the equilibrium tide. *Astronomy and Astrophysics*, 220:112–116, 1989.

J-P Zahn. Circulation and turbulence in rotating stars. *Astronomy and Astrophysics*, 265:115–132, 1992.

A. Geometry of equipotential integrations

In this appendix, some of the integration formulas are derived and some problems with the geometrical configuration are discussed. The equipotential surfaces

$$\Psi(x, y, z) = \frac{2}{1+q} \frac{1}{(x^2 + y^2 + z^2)^{1/2}} + \frac{2q}{1+q} \frac{1}{[(x-1)^2 + y^2 + z^2]^{1/2}} +$$
$$\left(x - \frac{q}{1+q}\right)^2 + y^2 = C \tag{A.1}$$

of the Roche model are fundamental to our analysis. In our work, we are primarily interested in a subset determined by C ranging from infinity to C_2 that corresponds to the second Lagrangian point L_2. The second parameter q, the mass ratio of the two stars in the binary, is a positive real number (Eq. (2.16)).

Given a point (x, y, z) at the equipotential, we define local acceleration in a usual way as a gradient of Ψ. The corresponding norm reads (Eq. (2.3))

$$g = \|\nabla\Psi\| = \sqrt{(\Psi_{,x})^2 + (\Psi_{,y})^2 + (\Psi_{,z})^2}, \tag{A.2}$$

where the indexes denote the partial derivative along the three Cartesian axes (i.e., $\Psi_{,x} = \partial\Psi/\partial x$, etc.). The value of g is always nonzero except the five critical points of the equipotentials, including L_1 and L_2 relevant for our work. Conceptually, these points are equilibria for a test mass, where the gravitational attraction by the primaries is compensated by the centrifugal effects if the rotating frame. We easily obtain

$$\Psi_{,x} = 2\left(x - \frac{q}{1+q}\right) - \frac{2}{1+q}\left\{\frac{x}{(x^2 + y^2 + z^2)^{3/2}} + \frac{q(x-1)}{[(x-1)^2 + y^2 + z^2]^{3/2}}\right\},$$
$$\Psi_{,y} = 2y - \frac{2y}{1+q}\left\{\frac{1}{(x^2 + y^2 + z^2)^{3/2}} + \frac{q}{[(x-1)^2 + y^2 + z^2]^{3/2}}\right\}, \tag{A.3}$$
$$\Psi_{,z} = -\frac{2z}{1+q}\left\{\frac{1}{(x^2 + y^2 + z^2)^{3/2}} + \frac{q}{[(x-1)^2 + y^2 + z^2]^{3/2}}\right\}.$$

Note that roots of $\Psi_{,x} = 0$, when $y = z = 0$, provide location of the three Lagrangian colinear points L_1 to L_3. While analytic solutions are available in the form of convergent series [e.g., Szebehely, 1967], it is more efficient to determine them numerically (especially for q values not too different from unity).

The Kippenhahn approach requires equipotential averages Eq. (2.1) to be computed. Following Mochnacki [1984], we actually switch from Cartesian coordinates (x, y, z) to a set of cylindrical coordinates (x, ρ, ϕ) such that (i) x defines the symmetry axis, (ii) ρ is the distance from x, and (iii) ϕ is the polar angle reckoned from z, i.e., $y = \rho\sin\phi$ and $z = \rho\cos\phi$ (implying $y^2 + z^2 = \rho^2$). With that choice, the equipotentials in Eq. (A.1) become functions of the cylindrical coordinates $\Psi(x, \rho, \phi)$ obeying symmetries expressed by mirror reflections $y \to -y$ and $z \to -z$, though not the axial symmetry.

Evaluation of the surface integrals Eq. (2.1) requires a choice of two independent curvilinear coordinates on the equipotential. Although these may be general, we

follow Mochnacki [1984] the coordinates (x, ϕ) to also be the parameters of the equipotential, thus $d\sigma = s(x, \phi)\,dxd\phi$ with some surface element function $s(x, \phi)$. Using standard tools of analytical geometry of surfaces in three-dimensional space, we obtain

$$s(\phi, x) = -\frac{g(\phi, x)\rho(\phi, x)}{\Psi_{,y}\sin\phi + \Psi_{,z}\cos\phi}, \qquad (A.4)$$

where g is the acceleration from (A.2), and the denominator may actually be also expressed as $\Psi_{,\rho}$. In fact, this result may be straightforwardly obtained using the following simple argument. The surface element oriented outward from the symmetry axis has an area $\rho\,dxd\phi$ and outward normal $\mathbf{n}_c = (0, \sin\phi, \cos\phi)$. Normal to the equipotential is $\mathbf{n}_s = -\nabla\Psi/g$, where $\nabla\Psi = -(\Psi_{,x}, \Psi_{,y}, \Psi_{,z})$ (note that the C constant decrease outward the star and then the outward normal should have the sign minus). The infinitesimal area on the equipotential surface thus reads (note the cosine of the tilt angle between the two unit vectors in the denominator)

$$d\sigma = \frac{\rho\,dxd\phi}{\mathbf{n}_c \cdot \mathbf{n}_s} = s(\phi, x)\,dxd\phi. \qquad (A.5)$$

As noted in Sec. 2.3.1, each equipotential $\Psi(x, \rho, \phi) = C$ intersects the symmetry axis x at two points $(x_{\min}, x_{\max})$ for all C values. The value $x_{\min}$ is always negative, and this intersection is located on the symmetry axis in a direction opposite to L_2. The intersection $x_{\max}$ is always positive, and may be localized in between the primaries (for $C > C_1$, i.e., detached configuration), or beyond the secondary (for $C < C_1$, i.e., common envelope configuration). Having a closer look at behaviour of the denominator of $s(\phi, x)$ in Eq. (A.4) near the intersection $x_{\min}$, we obtain

$$\Psi_{,y}\sin\phi + \Psi_{,z}\cos\phi \simeq 2\rho\left[\sin^2\phi - \frac{1}{1+q}\left(\frac{1}{r_1^3} + \frac{q}{r_2^3}\right) + O\left(\rho^2\right)\right], \qquad (A.6)$$

where $r_1 = |x_{\min}|$ and $r_2 = 1 + |x_{\min}|$ are distances from the primaries. At the limit $\rho \to 0$ the evaluation of the elementary surface area $d\sigma$ becomes inaccurate, because $s(\phi, x)$ suffers divergence, especially for large q. This is because the ρ factor cancels in the numerator and denominator, and the first two terms in the bracket on the right hand side of Eq. (A.6) may cancel. This is obviously a simple coordinate singularity, because approaching $x \to x_{\min}$ requires $dx \to 0$ in $d\sigma$. Interestingly, this problem has not been reported in Mochnacki [1984], most likely because of his choice of a too restricted range of q values.

The problem is removed by choosing a more suitable couple of curvilinear coordinates on the equipotential near the surface intersection at $x_{\min}$. For instance, we may keep using the cylindrical coordinates, but now set (ρ, ϕ) to act as the surface coordinates. In this case, $x(\rho, \phi)$ is the dependent coordinate on the equipotential, and $d\sigma = s'(\rho, \phi)\,d\rho d\phi$. The simple argument as above yields in this case $s'(\rho, \phi) = g\rho/\Psi_{,x}$.

Computation of the equipotential volume V_ψ (the first equation in (2.18)), and thus the equivalent radius $r_\Psi \propto V_\Psi^{1/3}$, is an easier task. For obvious reasons a number of researchers focused mainly on the case of the inner critical Roche lobe at $F = 1$. Starting from Kopal [1959], others like Eggleton [1983] or Leahy and Leahy [2015], have searched an approximate analytical formulation for $r_\Psi(q, F = 1)$
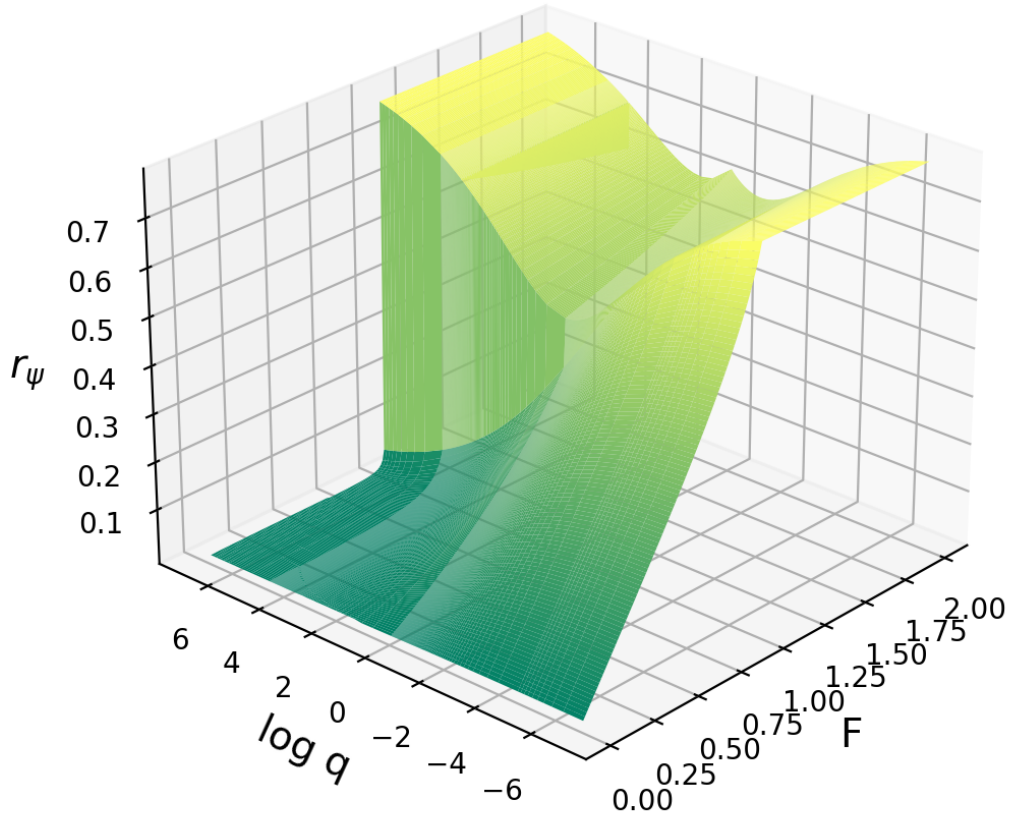
Figure A.1: The calculated table of equivalent radii r_Ψ of equipotentials of the Roche potential as a function of mass ratio $\log q$ and fill-out factor F (the values of r_Ψ are non-dimensional, scaled by the distance d of the components of the binary). This table is used for determining the appropriate fill-out factor.

that would closely match the numerically determined values (for instance near $q = 1$ a linear approximation $r_\Psi(q, F = 1) \simeq 0.38 - 0.2 \log q$ appears to hold well). Here we computed $r_\Psi(q, F)$ for a wide range of q values and also for the fill-out factors in its complete interval of values in between 0 and 2. Results are shown in Fig. A.1.

There are notable features that help us verify our results. For instance, very near the primary the equipotentials are little spheres and then $r_\Psi(q, F) \propto F$ in the limit of very small F. Obviously, the slope of this linear relation decreases with increasing $\log q$. At $F = 1$ our results favourably match those of Leahy and Leahy [2015]. There is obviously always a jump in $r_\Psi(q, F)$ when F crosses unity, as the equipotential volume instantly increases by that of the secondary Roche lobe. This is most significant for large $\log q$ values. Finally, $r_\Psi(q, F)$ beyond the inner critical Roche equipotential, i.e. $F > 1$, is symmetric under the $\log q \to -\log q$ transformation (see discussion in Sec. 2.2).

B. MESA inlists and functions

For reasons of the reproducibility of results, some of the additional MESA inlists are presented in this appendix.

B.1   Generating initial models

A sample appropriate inlist for generating initial models is:

```
&star_job
   ! see star/defaults/star_job.defaults

   ! begin with a pre-main sequence model
     create_pre_main_sequence_model = .false.

   ! save a model at the end of the run
     save_model_when_terminate = .true.
     save_model_filename = '10M_mid_MS.mod'

   ! display on-screen plots
     pgstar_flag = .true.

/ ! end of star_job namelist


&eos
   ! eos options
   ! see eos/defaults/eos.defaults

/ ! end of eos namelist


&kap
   ! kap options
   ! see kap/defaults/kap.defaults
   use_Type2_opacities = .true.
   Zbase = 0.02

/ ! end of kap namelist


&controls
   ! see star/defaults/controls.defaults

   ! starting specifications
     initial_mass = 1.0 ! in Msun units
     initial_z = 0.02

   ! options for energy conservation (see MESA V, Section 3)
      use_dedt_form_of_energy_eqn = .true.
      use_gold_tolerances = .true.

   ! stop when the star nears ZAMS (Lnuc/L > 0.99)
     Lnuc_div_L_zams_limit = 0.99d0
     stop_near_zams = .false.
     max_num_profile_models = 1000

   ! stop when the center mass fraction of h1 drops below this limit
     xa_central_lower_limit_species(1) = 'h1'
     xa_central_lower_limit(1) = 0.3
     profile_interval=1

/ ! end of controls namelist
```

B.2 Relaxation

A sample appropriate inlist for relaxation procedures is:

```
&star_job
   ! start a run from a saved model
     load_saved_model = .true.
     saved_model_name = '10M_mid_MS.mod'
     initial_model_relax_num_steps = 20


   ! save a model at the end of the run
     save_model_when_terminate = .true.
     save_model_filename = '1M_mid_MS_relaxed.mod'

   ! display on-screen plots
    pgstar_flag = .true.

    new_rotation_flag = .true.
    change_rotation_flag = .true.

/ ! end of star_job namelist

&kap
   ! kap options
   ! see kap/defaults/kap.defaults
   use_Type2_opacities = .true.
   Zbase = 0.02

/ ! end of kap namelist

&controls
   ! see star/defaults/controls.defaults

   ! options for energy conservation
     use_dedt_form_of_energy_eqn = .true.
     set_uniform_am_nu_non_rot = .true.
     uniform_am_nu_non_rot = 1d20
     use_gold_tolerances = .true.

   ! stop when the star nears ZAMS (Lnuc/L > 0.99)
     max_age=5.1432259550089808E+009
     Lnuc_div_L_zams_limit = 0.99d0
     stop_near_zams = .false.

     use_other_eval_fp_ft = .true.
     use_other_surface_PT = .true.
     dxdt_nuc_factor = 0

     max_years_for_timestep=8.586525952265069E+006
     profile_interval = 1
     force_timestep_min_years=1e5
     force_timestep_min_factor=3
     max_num_profile_models=500

/ ! end of controls namelist
```